Stress-induced ribosome degradation in *Bacillus subtilis* is mediated by the RNase Y-specificity complex.

Fabián A. Cornejo[1,*], Kristina Driller[1,2,*], Rina Ahmed-Begrich[1], Katja Schmidt[1], Michael Jahn[1], Vivekanandan Shanmuganathan[1], Karin Hahnke[1], Florian Kondrot[1], Thomas F. Wulff[1], Sebastian Rämisch[1], Kathirvel Alagesan[1], Emmanuelle Charpentier[1,3], and Kürşad Turgay[1,2]

[1]Max Planck Unit for the Science of Pathogens, Berlin, Germany

[2]Leibniz Universität Hannover, Institute of Microbiology, Hannover, Germany

[3]Humboldt-Universität zu Berlin, Institute of Biology, Berlin, Germany

* These authors equally contributed to this work

Correspondence to: cornejo@mpusp.mpg.de, turgay@mpusp.mpg.de

Abstract

Limiting the synthesis and activity of ribosomes is crucial for adaptation to stresses, such as heat or nutrient starvation. In *Bacillus subtilis,* this can be achieved through the coordinated action of the alarmones (p)ppGpp and the transcription factor Spx. Here, we performed a genetic screen to uncover novel factors contributing to the heat shock response of *B. subtilis*. We identified the Y-complex, which confers specificity to the endonuclease RNase Y, as a critical player during stress conditions, such as heat or transition into stationary phase. This protein complex is required for processing diverse RNAs, notably the maturation of mRNAs encoding proteins involved in translation and metabolism. We further demonstrate that the Y-complex and RNase Y initiate the degradation of rRNAs of mature ribosomes, lowering their abundance. We propose that the Y-complex is a regulatory hub that modulates gene expression, adjusts protein synthesis and resource allocation.

Keywords: *Bacillus subtilis*, Ribosome, Stress response, Y-complex, RNase Y, Ribosome degradation, Heat shock, (p)ppGpp

Introduction

Bacteria can sense, adapt to, and survive stressful environmental changes facilitated by various general and specific stress response systems. Proteotoxic stresses, like high temperatures, significantly disrupt protein folding and can lead to the formation of toxic protein aggregates. Chaperones and proteases are expressed as a response due to the inactivation of the transcriptional repressors HrcA and CtsR in *Bacillus subtilis*[1–4]. The activation of the protein quality control (PQC) allows the refolding of un- or misfolded proteins by different chaperone systems or the degradation of irreparable proteins through AAA+ protease complexes like ClpCP[5,6].

In addition to the repairing or removal of protein aggregates, inhibiting translation is crucial for survival during proteotoxic stresses, as it can alleviate the extra load on the PQC system[7–10]. In *Bacillus subtilis*, the nucleotide second messengers guanosine tetraphosphate and guanosine pentaphosphate, collectively referred to as (p)ppGpp, and the transcription factor Spx independently regulate synthesis and activity of ribosomes during stress[7,11]. Spx is a redox-sensitive heat shock transcription factor that controls the expression of redox chaperones and simultaneously represses transcription of translation-related genes during oxidative and heat shock response[11–14].

The alarmones (p)ppGpp were initially discovered to be synthesized during amino acid starvation, but more recently, it was observed that their synthesis is also induced by protein folding stresses, such as heat or oxidative stress[7]. During heat stress, their accumulation results in increased thermoresistance, inhibition of translation, and a reduction in protein aggregation[7]. (p)ppGpp inhibit translation by binding to specific GTPases (e.g. IF2, RbgA)[15–17]. Furthermore, (p)ppGpp accumulation can lead to decreased transcription of e.g. rRNA and ribosomal protein (r-protein) transcripts by inhibiting GTP biosynthesis and reducing its levels[18,19]. This downregulation of translation is an important component of the response to nutrient scarcity as well as heat shock.

In this study, we aimed to identify new genes or pathways involved in the heat shock response using a genetic screen that reports on fitness. We identified that the Y-complex (RicAFT-complex), which interacts with the endonuclease RNase Y and conveys substrate specificity, plays a role in the heat shock response. We demonstrate further that the Y-complex regulates ribosome levels by initiating ribosome degradation during nutrient depletion or heat shock. Mutants lacking a Y-complex member show increased ribosome levels before and during heat shock, increasing the burden on the PQC system and, in consequence, protein aggregation during heat stress. These findings not only indicate the importance of RNases during stress response but also emphasize that controlling the stability of RNA is an important general mechanism to modify cellular function.

Results

The Y-complex is necessary for survival during heat shock

To identify genes that play a role in the heat shock response, we used the BKE single-mutant library[20], which includes a barcoded deletion cassette for each non-essential gene in *B. subtilis*. All gene deletion mutant strains were pooled, grown at 30°C, and subjected to a mild heat shock at 50°C during the mid-exponential phase, while a control was maintained at 30°C. Relative fitness scores for each gene deletion in the pooled population were calculated by quantifying each barcode at different temperatures (**Fig. 1A, Table S1**). The relative fitness of the heat shocked cultures compared to the cultures grown at 30°C was used to identify genes whose deletion results in a change in fitness during heat shock (**Fig. 1A-B, Table S1**).

We observed that *B. subtilis* strains lacking the genes coding for the heat shock transcriptional repressors HrcA or CtsR exhibit higher fitness at 50°C compared to 30°C (**Fig. S1A**), consistent with their known regulatory role. In contrast, deletion of the genes coding for the DnaK chaperone system, the protease ClpP, and the adaptor protein complex McsA-McsB show greater sensitivity to increased temperatures (**Fig. S1B**), demonstrating that our screening approach can identify genes with already known heat-shock phenotypes[21–23].

The control of transcription initiation by transcription factors has been well established[24]. However, the contribution of RNA stability in stress response is not well understood. Interestingly, six mutants lacking RNases or RNase-regulating genes exhibit differential fitness at 50°C compared to 30°C (**Fig. 1B)**. The deletion of RNase Mini-III (Δ*mrnC)* results in lower fitness at 30°C, whereas its fitness remains unaffected at 50°C. Deletions of RNase J2 (Δ*rnjB)*, the nano-RNase A (Δ*nrnA*), and the RNA pyrophosphohydrolase and (p)ppGpp hydrolase NahA (Δ*yvcI*) exhibit reduced fitness during increased temperatures (**Fig. 1B**).

One of the mutants with the lowest fitness score at 50°C is Δ*ymcA* (**Fig. 1B**). YmcA (RicA) interacts with YaaT (RicT) and YlbF (RicF) to form the Y-complex, which associates with the endonuclease RNase Y for maturation of polycistronic mRNA and riboswitches[25,26]. In addition, we also identified Δ*yaaT* in our screen (**Fig. 1B**). We could confirm the heat sensitivity of all three deletion mutants of the Y-complex genes in single-culture experiments during a severe heat shock at 54°C (**Fig. 1C**).

Identification of Y-complex-dependent cleavages at late exponential and transition phases

We evaluated the growth of all three strains lacking the Y-complex encoding genes. They exhibit a similar growth defect that begins at the end of the exponential phase and continues during transition phase until the stationary phase (**Fig. 2A**)**.** Given that this complex associates

97 with the endonuclease RNase Y and regulates substrate selection[26], we investigated Y-
98 complex-dependent cleavages in the late exponential and transition phase (**Fig. 2A**) using the
99 ISCP (Identification of Specific Cleavage Positions) approach[27]. We compared the coverage
100 of RNA 3' and 5' ends in the WT and Δ*ymcA* mutant, and the ends significantly reduced in the
101 Δ*ymcA* were classified as putative Y-complex-dependent cleavages (**Table S2**). It is worth
102 noting that deleting any member of the Y-complex results in a significant decrease in the
103 processing of substrate RNA[26]. When a transcript is cleaved, it results in two products: one is
104 quickly degraded by exonucleases, while the other is stabilized[27]. Consequently, it is not
105 always possible to detect both 5' and 3' ends after cleavage.

106 We identified 221 and 258 Y-complex-dependent ends in late exponential and transition
107 phases, with six also detected in a previous study at the mid-exponential phase[26] (**Table S3**).
108 In the late exponential phase, 5' and 3' ends are almost equally distributed, yet more 5' ends
109 are detected in the transition phase (**Fig. 2B**).

110 It is known that the Y-complex and RNase Y generate fragments with differential stability in the
111 mid-exponential phase[26]. Here, we evaluated the stability of the resulting fragments in the late
112 exponential and transition phases by calculating the ratio of coverage upstream and
113 downstream of the cleavage site (**Table S2**). We observed a trend toward stabilizing
114 downstream fragments. However, upstream fragments can also be stabilized, but to a lesser
115 extent (**Fig. S2A**). The ISCP method differentiates processing sites with blunt ends (Unique,
116 U-type) or when it was further processed by exonucleases[27] (Stepped, S-type). Most S-types
117 were found at the 3' ends, suggesting further processing by exonucleases, while most U-types
118 were detected at 5' ends (**Fig. 2C**). This is consistent with the trend to stabilise the downstream
119 fragment (**Fig. S2A**).

120 The Y-complex could target a particular sequence motif, thereby helping to recognize specific
121 substrates. However, a motif search using U-type ends resembles the simple motif described
122 for RNase Y in *B. subtilis*[28], *S. aureus*[29], and *S. pyogenes*[27], being most likely a G upstream of
123 the cleavage site (**Fig. S2B**). Given the simple sequence motif, we investigated whether
124 cleavages occur randomly in longer or more abundant transcripts. Notably, approximately 81%
125 of targeted transcripts are cleaved only once, about 16% twice, and very few are cleaved
126 multiple times (**Fig. S2C)**. Neither the length nor the abundance of a transcript predicts whether
127 it is cleaved, suggesting that other factors influence where cleavages occur (**Fig. S2D-E, Table**
128 **S4**). Recent studies have shown that the cleavage efficiency is multifactorial, depending on
129 the sequence and secondary structures surrounding the cleavage site[28,30].

130 As we observed that RNA processing could result in fragments with different stability (**Fig.**
131 **S2A**), we wondered if this could be a consequence of secondary structures protecting them
132 from exonucleases. We used U-type ends and compared transcripts with the same cleavage

133 motif but not cleaved as controls. For the 5' ends, a strong decrease in the minimum free
134 energy ~25 nt downstream of the cleavage site indicated a possible secondary structure, while
135 the upstream fragment remained similar to the control (**Fig. 2D**). The upstream fragment's
136 lower stability may be due to its lack of secondary structure, making it accessible to 3'-5'
137 exonucleases. For the 3' ends, the more stable upstream fragment could form a possible
138 secondary structure starting 10 nt upstream of the cleavage site (**Fig. 2D**). The generation of
139 mRNA fragments with different stability might have a regulatory role in gene expression.

140 **Y-complex-mediated transcript cleavages and mRNA maturation**

141 Most detected Y-complex-dependent ends are inside ORFs, mainly in polycistronic mRNAs
142 (**Fig. 2E-F**), confirming the role of the Y-complex in the maturation and stoichiometry regulation
143 of co-transcribed genes[26]. An example is the *cggR-gapA* transcript, where the Y-complex
144 mediates cleavage in the coding sequence of *cggR* near the stop codon[25,26]. Cleavage renders
145 the *cggR* fragment less stable compared to the *gapA* fragment (**Fig. S3A**), thereby uncoupling
146 the transcript levels of these co-transcribed genes. Interestingly, we observed other cleavages
147 generating similar uncoupling of transcripts, such as in the gene encoding the endonuclease
148 YloC (**Fig. S3B**, **Table S2)**. In addition, cleavages in genes transcribed as monocistronic
149 mRNAs, such as *guaB,* suggest that the Y-complex could initiate their degradation (**Fig. S3C**,
150 **Table S2**).

151 We observe Y complex-dependent processing in 5', 3', and internal UTRs (**Fig. 2F**). Cleavages
152 in 5' UTR suggest a possible regulatory role by decreasing the abundance of the mRNA
153 containing them, as already described for riboswitches[26,31], or by producing a shorter version
154 of a 5' UTR, which could affect gene expression. Processing of 3' and internal UTR could
155 influence mRNA stability and polycistronic mRNA maturation. We observed that some 3' UTR
156 cleavages are located upstream of the Rho-independent terminator, decreasing the stability of
157 the upstream fragment and leaving an apparent more stable downstream fragment that
158 includes its terminator structure, as observed for *trxB* (**Fig. S3D**). This phenomenon has been
159 observed in *E. coli*, where RNase E cleaves upstream of the Rho-independent terminator[32,33].

160 In polycistronic mRNA maturation, we observed that Y-complex processes internal UTRs,
161 decoupling the RNA levels of coding fragments (**Fig. S3E-F**). For example, the *bipA-ylaH*
162 transcript is cleaved 21 nt after the *bipA* stop codon, rendering the upstream fragment less
163 stable than the *ylaH* fragment (**Fig. S3E**). We also observed a cleavage between the *fusA* (EF-
164 G) and *tufA* (EF-Tu) genes, both coding for translation elongation factors (**Fig. S3F**).

165

166

167 **The Y-complex targets translation and metabolism-related genes in the late exponential**
168 **phase**

169 We wondered if the Y-complex primarily processes transcripts bearing genes with specific
170 functions required for switching the growth phase. Therefore, we conducted an
171 overrepresentation analysis and observed that the most significantly enriched categories
172 pertain to "Metabolism" and "Information processing" (**Fig. 2G, Fig. S4A, Table S5**). Overall,
173 the Y-complex is predominantly involved in the processing of operons encoding genes for
174 carbon metabolism (e.g., glycolysis and gluconeogenesis), nucleotide metabolism (e.g.,
175 pyrimidine and purine biosynthesis), and amino acid biosynthesis and utilization (**Fig. 2G**). This
176 allows adjusting the utilization and biosynthesis of nutrients when they become limited. In
177 addition, all transcripts containing rRNA and ~50% of transcripts carrying genes encoding
178 translation factors and r-proteins are processed by the Y-complex (**Fig. 2G**).

179 The reduced RNA processing in the *ymcA* deletion strain results in significant changes in the
180 transcriptome (**Fig. S4B, Table S6-7**). Consequently, transcripts of certain pathways related
181 to metabolism and translation, among others, show maturation events that depend on the Y-
182 complex and also demonstrate differential expression upon deletion of *ymcA* (**Fig. 2G**, **Fig.**
183 **S4B**). This may result from either a direct or indirect effect of decreased RNA maturation
184 events. Our results suggest that the Y-complex and RNase Y are important for transitioning to
185 the stationary phase by processing transcripts related to translation and metabolism, which
186 may impact their stability and/or gene expression.

187 **The Y-complex targets ribosomes for degradation**

188 Several Y complex-dependent cleavages were detected in the rRNA sequence during both
189 growth phases, most of them being in the 23S rRNA during the late exponential phase (**Fig.**
190 **3A**). We detected cleavages in specific helices in the 23S and 16S rRNA, mainly in loops of
191 hairpin structures (**Fig. S5A-B**). These helices are accessible and primarily located close to
192 the A-site and the interface between the two ribosomal subunits (**Fig. S6**), which could be
193 recognized and cut by the Y-complex with the endonuclease RNase Y. These cleavages will
194 most likely destabilize the ribosome structure. Generating free 5' and 3' RNA ends, which are
195 substrates for exonucleases such as PNPase, RNase R, and RNase J, will result in further
196 RNA degradation and ribosome disassembly, releasing the ribosomal proteins as well.

197 We confirmed the observed rRNA degradation via northern blots of 23S or 16S rRNA (**Fig. 3B**,
198 **Fig. S7A**). Deletion of *ymcA* strongly reduces the presence of rRNA degradation intermediates
199 during the late exponential phase. As ribosomes are assembled co-transcriptionally[34], we
200 inhibited transcription by adding rifampicin to cultures at the late exponential phase. We
201 observed that stopping transcription does not affect rRNA degradation of the 23S and even

202 raises the levels of 16S degradation intermediates, indicating that mature ribosomes are
203 degraded (**Fig. 3B**, **Fig. S7A**).

204 Cleavages within mature rRNA can trigger ribosome disassembly and degradation, which,
205 during the transition phase, coincides with translation downregulation through reduced
206 synthesis and inhibition of ribosome activity. This suggests that the Y-complex may be involved
207 in reducing ribosome levels to accommodate the new, slower growth rate. Therefore, we
208 quantified ribosome content by measuring the abundance of all r-proteins via mass
209 spectrometry (**Table S8**). When *B. subtilis* shifts from exponential to the transition phase, we
210 observed a coordinated reduction in r-protein levels (**Fig. 3C**), indicating a decrease in
211 ribosome levels. This reduction is highly impaired in Δ*ymcA* (**Fig. 3C**), where the levels of r-
212 proteins do not decline to the same degree as in the WT, likely due to the reduced degradation
213 of ribosomes.

214 Accumulation of (p)ppGpp leads to inhibition of transcription of rRNA and r-proteins[19,35] upon
215 shortages of nutrients during the transition to the stationary phase. To test if the deletion of
216 *ymcA* is interfering with this transcriptional downregulation, we measured the promoter activity
217 of the rRNA promoters *rrnJ* and *rrnB* and r-protein promoters of *rplK*, *rplJ*, and *rpsJ*. All these
218 promoters show similar downregulation in the late exponential and transition phases in both
219 WT and Δ*ymcA* strains (**Fig. 3D-E**, **Fig. S7B-D**), confirming that their transcriptional control
220 remains unaffected and is not the cause of the increased ribosome amounts in the Δ*ymcA*
221 strain.

222 Notably, we observed that the increased levels of ribosomes in a Δ*ymcA* strain led to the
223 accumulation of hibernating 100S ribosomes during the transition phase (**Fig. 3F**). This 100S
224 is no longer observed after the deletion of the gene encoding the hibernation factor *hpf*, which
225 triggers their formation[36,37] (**Fig. S7E**). The presence of hibernating ribosomes at this time point
226 indicates that functional and superabundant ribosomes in the Δ*ymcA* strain are sequestered
227 away from the actively translating pool through hibernation.

228 **(p)ppGpp and the Y-complex play a crucial role in regulating the levels of ribosomes**

229 Since ribosome levels and translation are lowered by (p)ppGpp under nutrient limitation or
230 other stresses, we wondered if there is a genetic interaction between the two systems. Deleting
231 *ymcA* in a strain that cannot synthesize (p)ppGpp [(p)ppGpp^0] leads to an even stronger growth
232 defect during the transition phase (**Fig. 4A**). The (p)ppGpp^0 strain, like Δ*ymcA*, shows impaired
233 reduction of ribosome levels during the transition phase (**Fig. 4B**). The double mutant
234 (p)ppGpp^0 Δ*ymcA* shows almost no reduction in ribosome quantities during this growth phase
235 (**Fig. 4B-C**). The same is observed when the r-protein mass fraction is calculated at the
236 transition phase (**Fig. 4D**). These experiments suggest that the Y-complex and (p)ppGpp

237 control ribosome levels and translation independently during post-exponential growth. The
238 absence of regulation by both systems results in a severe growth defect.

239 **Increased ribosome levels lead to protein aggregation during heat shock**

240 Since we discovered the Δ*ymcA* strain in a competition experiment during heat shock, we
241 explored whether the Y-complex is involved in lowering ribosome levels upon proteotoxic
242 stress. We evaluated the degradation of 23S and 16S rRNA by the Y-complex before and after
243 heat shock (**Fig. 5A**, **Fig. S8A**). After 15 minutes at 50°C, degradation intermediates are
244 observed in the WT but not in Δ*ymcA*, confirming a role of the Y-complex in degrading
245 ribosomes during heat stress (**Fig. 5A**). Comparing r-protein mass fractions before and during
246 heat shock shows that both WT and Δ*ymcA* downregulate ribosome levels during the
247 experiment. Overall, there are increased levels of r-proteins in the Δ*ymcA* strain already before
248 the heat shock (**Fig. 5B**), which suggests a role of the Y-complex in maintaining ribosome
249 levels during normal growth. Notably, the levels and induction of known heat-shock-regulated
250 proteins are not affected in the *ymcA* deletion (**Fig. 5C, Table S9, Fig. S8B**). This suggests
251 that chaperone and protease induction during heat stress in the Δ*ymcA* strain is intact.

252 The downregulation of translation is crucial to limit the increased burden of misfolding and
253 aggregation-prone nascent polypeptide chains on the PQC system. In agreement, a (p)ppGpp^0
254 strain shows increased aggregate formation during heat shock[7]. We quantified the relative
255 amount of aggregated proteins before and after 15 minutes of severe heat shock at 54°C and
256 observed that the Δ*ymcA* strain contained significantly higher amounts of aggregated proteins
257 already prior to heat exposure (**Fig. 5D**). This is consistent with the observed increased
258 ribosome levels of the Δ*ymcA* strain already without heat shock (time point 0 in **Fig. 5B**). After
259 15 minutes of heat shock, Δ*ymcA* shows 20% more aggregated proteins than WT. The
260 (p)ppGpp^0 Δ*ymcA* mutant exhibits even higher protein aggregation than Δ*ymcA* or (p)ppGpp^0
261 strains alone, further supporting that (p)ppGpp and the Y-complex act independently on the
262 regulation of ribosome levels and translation (**Fig. S8C**). Mutants of the Y-complex are also
263 strongly affected by other proteotoxic stresses, such as osmotic and oxidative stress, but not
264 by ethanol (**Fig. S8D**), which further demonstrates the importance of controlling ribosome
265 levels under proteotoxic stress conditions.

266 We observed that the Y-complex globally controls the RNase Y-mediated maturation of
267 transcripts and is involved in adjusting ribosome levels to the growth state, allowing the
268 endonuclease RNase Y to initiate the processing and degradation of rRNA and r-protein
269 transcripts. The absence of the Y-complex results in an abundance of idle ribosomes, which
270 interfere with the downregulation of translation and increase sensitivity to protein folding
271 stresses.

272 **Discussion**

273 Bacterial adaptation to environmental challenges depends on their ability to quickly change
274 gene expression. Beyond the well-known regulation of transcription initiation, we observed
275 here that post-transcriptional mechanisms, which influence RNA stability or translation
276 efficiency, also contribute to the rapid and tailored cellular response. In this context, the control
277 of RNases plays a critical role, since we show that the fitness of *B. subtilis* during heat shock
278 is critically dependent on certain non-essential RNases and the Y-complex, which controls the
279 substrate selection of the quasi-essential endonuclease RNase Y[26] (**Fig. 1B-C**). Together, our
280 findings demonstrate that the Y-complex – RNase Y system is a regulatory hub that modulates
281 gene expression and the cell's translational capacity during stress response.

282 Our RNA-seq analyses reveal that the Y-complex may regulate transcripts involved in a wide
283 range of metabolic pathways, developmental processes, stress responses, and translation
284 (**Fig. 2G, Fig. S4A-B, Table S2, Table S6-7**). RNA processing by the Y-complex-guided
285 RNase Y can create new transcript isoforms[26] or modify regulatory elements such as
286 UTRs[26,31](**Fig. 2F**, **Fig. S3**), thereby tailoring gene expression to specific growth conditions.
287 This wide regulatory scope of the Y-complex could explain the known pleiotropic phenotypes
288 in these mutants, like decreased sporulation, competence, and defective biofilm formation[38–
289 40].

290 Among these diverse functions in RNA processing, we discovered that the Y-complex initiates
291 ribosome degradation at the end of exponential growth by directing RNase Y to cleave 23S
292 and 16S rRNA (**Fig. 3A-B**, **Fig. S7A**), thereby decreasing the levels of ribosomes. This finding
293 is consistent with previous suggestions that RNase Y can degrade rRNA in aging *B. subtilis*
294 spores[41].

295 The exact nature of how the Y-complex (YmcA, YlbF, and YaaT) associates with RNase Y is
296 an active subject of research. Recent evidence indicates that YmcA and YlbF transfer YaaT to
297 RNase Y, forming a stable, membrane-localized YaaT-RNase Y complex[42]. However, the
298 deletion of any of the Y-complex members leads to a strong decrease in the processing of
299 target mRNA[26], indicating that all Y-complex proteins are equally indispensable for RNA
300 processing. Based on the dynamic localization of YmcA and YlbF between the cell membrane
301 and the cytosol[43], we propose that these Y-proteins may also recognize substrates, including
302 ribosomes, and direct them to RNase Y for cleavage.

303 The two $[4Fe\text{-}4S]^{+2}$ clusters in the Y-complex[44] likely act as sensors for cellular growth, energy,
304 and stress, affecting how the complex controls RNase Y. This regulatory complex is localized
305 at the cell membrane, where RNase Y forms a dynamic degradosome-like network with other
306 RNases, helicases, and glycolytic enzymes[45–47]. This spatial co-localization may enable a

307 sequential degradation process: the Y-complex-guided RNase Y performs initial cleavage on
308 targets like rRNA, making fragments susceptible to further degradation by exonucleases such
309 as RNase R, PNPase, and RNase J. This suggests complex spatial control of RNA processing
310 and ribosome decay, separate from transcription and translation in the cytoplasm (**Fig. 6**).

311 Most of the cleavages we observed in rRNA were in the 23S (**Fig. 3A**); however, the Y-complex
312 and RNase Y can also initiate 16S degradation in the late exponential phase and during heat
313 shock (**Fig. 3A**, **Fig. S7A**, **Fig. S8A**). Recently, it was observed that the exoribonuclease
314 RNase R alone can degrade 16S[48], suggesting that endonucleolytic cleavages might not be
315 strictly necessary for 16S degradation. Since RNase R is induced as part of the general stress
316 response[49], it suggests a possible stress-specific and Y-complex-independent degradation
317 pathway for 16S rRNA.

318 Complete ribosome decay requires the concurrent degradation of r-proteins (**Fig. 6**). These
319 proteins might be passively released from the ribosome into the cytoplasm during the
320 degradation of the rRNA. Since this would also change their interaction with rRNA, they might
321 misfold and aggregate, and can subsequently be degraded by AAA+ protease complexes.
322 Alternatively, these AAA+ protease complexes could be actively recruited to the site of
323 ribosome degradation to simultaneously extract and degrade the r-proteins along with rRNA.
324 AAA+ protease complexes such as ClpCP with McsB[50–52] or ClpXP, which functions in
325 ribosome-associated quality control in *B. subtilis*[53,54], could be involved in the proteolysis of the
326 released r-proteins.

327 Strikingly, our work reveals a second tier of regulation of ribosome levels. The Y-complex
328 additionally processes transcripts encoding r-proteins and other translation factors (**Fig. 2G**),
329 such as BipA, EF-Tu, and EF-G (**Fig. S3E-F**), potentially regulating their translation or leading
330 to their decay. This is supported by the findings that the Y-complex is necessary to process
331 some r-protein transcripts at the mid-logarithmic phase[26], and RNase Y depletion in this growth
332 phase leads to an increased abundance of transcripts of r-proteins, such as *rplS, rpsO, rpmA,*
333 *rpsD, rpsB,* and *rplU*[55].

334 The control of translation is an important component of many stress response mechanisms.
335 During nutrient starvation, downregulating translation allows the reallocation of resources to
336 biosynthetic pathways[56]. During proteotoxic stresses, it could relieve the overwhelmed PQC
337 system by reducing the synthesis of new proteins that could potentially aggregate[57]. The stress
338 transcription factor Spx and the alarmones (p)ppGpp regulate ribosome levels in *B. subtilis*,
339 and the lack of both impairs growth at 50°C[7]. Our work establishes a mechanistic link between
340 the regulation of ribosome levels through synthesis and decay. The severe growth defect
341 observed in cells lacking both (p)ppGpp and the Y-complex indicates that these systems are
342 important for transitioning from exponential to stationary phase. Furthermore, the absence of

343 their combined regulation of translation results in elevated ribosome levels and increased
344 accumulation of protein aggregates. (**Fig. S8C**). In times of nutrient limitation, the collective
345 function of (p)ppGpp and the Y-complex in regulating ribosome levels by inhibiting their
346 synthesis and initiating degradation allows resource allocation to other biosynthetic pathways
347 (**Fig. 6**).

348 These strategies are not exclusive to *B. subtilis*, as different organisms use various
349 mechanisms to degrade ribosomes. These must specifically recognize the ribosome or its
350 subunits to disassemble them and target rRNA and r-proteins for degradation. For example,
351 *E. coli* cells transitioning into the stationary phase also initiate ribosome degradation by the
352 membrane-associated endonuclease RNase E[58,59], which is functionally equivalent to RNase
353 Y in *B. subtilis*[60]. RNase E forms the scaffold of the membrane-associated degradosome
354 network in *E. coli*[61]. This could allow for the combined activity of endo- and exonucleases,
355 facilitating the full degradation of the ribosome[60,62]. In addition, it was observed that *E. coli* r-
356 proteins are degraded by the Lon AAA+ protease during starvation[63]. In eukaryotic cells,
357 nutrient starvation also triggers ribosome degradation via the ubiquitin-proteasome system or
358 via specialized autophagy pathways, such as ribophagy[64]. Recent studies have described how
359 stress- or starvation-induced degradation of the 40S ribosome involves the ubiquitylation of
360 proteins S3 and S5. This allows RIOK3 binding, leading to the decay of 18S rRNA by unknown
361 RNases[65–67].

362 In summary, we identified the Y-complex as a key regulator of ribosome abundance in *B.*
363 *subtilis*. The Y-complex regulates the translational activity by triggering ribosome decay and
364 processing transcripts for new ribosomal components. Our findings contribute to the
365 understanding of ribosome degradation by identifying a direct pathway and illustrating how this
366 process is integrated with other stress response mechanisms to control cellular growth and
367 survival. Further studies are required to understand the molecular signals that trigger ribosome
368 degradation and how the decay of rRNA and r-proteins is temporarily and spatially coordinated.

369

370 **Materials and methods**

371 Growth conditions

372 Unless stated the contrary, strains (**Table S10**) were streaked on LB plates (5 g/l yeast extract,
373 10 g/l tryptone agar, 10 g/l NaCl, 1.5% agar) containing the required antibiotics for selection (1
374 µg/ml erythromycin + 25 µg/ml lincomycin, 150 µg/ml spectinomycin or 10 µg/ml kanamycin)
375 and incubated overnight at 37°C. A single colony was inoculated in 3 ml of LB medium and
376 grown overnight at 37°C and 180 rpm, then used as the inoculum for subsequent experiments.

377 Strain construction

378 For constructing the strains Δ*ymcA::erm*^{R} and Δ*yaaT::erm*^{R}, the loci containing the resistance
379 cassette were PCR-amplified from the respective strains of the BKE library[20] and transformed
380 in *B. subtilis* WT. The deletions of Δ*rel::kan*^{R} and Δ*ylbF::erm*^{R} were constructed as described
381 in Ref.[20]. For promoter activity reporter strains, the *gfp*(mut2) gene was cloned downstream of
382 the promoters of interest, using the integrative plasmid pDR111 as a backbone.

383 For transformation, 600 µl of an overnight culture of the receptor strains were diluted in 5 ml
384 competence medium (17.5 g/l K_2HPO_4, 7.5 g/l KH_2PO_4, 2.5 g/l $(NH_4)_2SO_4$, 1.25 g/l tri-sodium
385 citrate x2 H_2O, 0.5% glucose, 7 mM $MgSO_4$, 0.1 mg/ml L-tryptophan, 0.02% casamino acids,
386 0.22 g/ml ammonium iron citrate) and grown at 37°C, 180 rpm, for 3 hours. Subsequently, 5
387 ml of starvation medium (17.5 g/l K_2HPO_4, 7.5 g/l KH_2PO_4, 2.5 g/l $(NH_4)_2SO_4$, 1.25 g/l tri-sodium
388 citrate x2 H_2O, 0.5% glucose, 7 mM $MgSO_4$) were added and grown for 2 more hours. One ml
389 of this culture was incubated with the DNA to be transformed and grown for 2 hours at 37°C
390 and 180 rpm. Positive clones were selected on LB agar containing the required antibiotics.
391 Genetic modifications were verified using PCR and DNA sequencing.

392 Genetic screening during heat shock

393 The BKE library[20] was replicated on LB agar plates containing 1 µg/ml erythromycin. Liquid
394 cultures were prepared in 200 µl LB medium supplemented with 1 µg/ml erythromycin and
395 grown for 42 hours at 30°C 200 rpm. All mutant strains were pooled and mixed for 15 minutes
396 using a magnetic stirrer. The pooled culture was centrifuged at 5000 rpm for 10 minutes at
397 18°C. The pellet was resuspended in LB medium to an OD_{600} of 65 and mixed with an equal
398 volume of 50% glycerol. The pooled library was aliquoted and kept at -80°C.

399 For each replicate, a tube of the pooled library was quickly unfrozen in a water bath at 30°C
400 and used to inoculate 75 ml LB medium in 500 ml flasks to a starting of OD_{600} 0.05. The culture
401 was grown in a water bath at 30°C, 180 rpm, until OD_{600} 0.4. Fifty ml of culture were split into
402 two 250 ml flasks. One flask was transferred to 50°C, 180 rpm for heat shock. The other flask
403 was used as a control sample and was kept at 30°C. One ml samples were collected for gDNA

404 purification at 0 and 2 hours post temperature shift. Samples were pelleted for 2 minutes at
405 13,000 rpm and washed once with 500 µl PBS. gDNA was purified using the Wizard® Genomic
406 DNA Purification Kit (Promega, A1120) and stored at -20°C until further processing.

407 The strain-specific barcodes were amplified using indexed primers (**Table S7**) with the Collibri
408 Library Amplification Master Mix (ThermoFisher, A38539050) according to the manufacturer's
409 instructions, with 100 ng of gDNA as input, for 22 cycles. Barcodes were gel-purified,
410 quantified, pooled equimolarly, and sequenced using the Illumina NovaSeq2 single-read
411 method at the Sequencing Core Facility of the Max Planck Institute for Molecular Genetics
412 (Berlin, Germany).

413 To calculate the fitness score of each deletion mutant from barcode abundance, BEAN-counter
414 v2.6.1[68] was used with the following settings. A fixed amplicon read structure was used with
415 an index at position 0, the common primer sequence GCAGGCGAGAAAGGAGAG at position
416 9, and the mutant barcode at position 27 of read 1. All other settings were used with default
417 values. The sample before heat shock served as a reference to which all other time points
418 were compared. All comparisons were performed with three biological replicates.

419 Fitness data was further analyzed using the R statistical computing language (v4.3.3). For
420 annotation, protein-related information was fetched using the Uniprot REST API (29 February
421 2024). Average fitness per gene, condition, and time point was calculated as the arithmetic
422 mean of the fitness score from three biological replicates. Differential fitness ΔF, e.g. for
423 comparison of treatment *versus* control at a particular time point, was calculated as $\Delta F =$
424 $F_{treatment} - F_{control}$. A two-sided Student's t-test was performed to evaluate statistical significance
425 for each gene, and the obtained *p*-value was corrected using the Benjamini-Hochberg
426 procedure[69].

427 Growth curves

428 Twenty-five ml of LB medium were inoculated with an overnight culture to a starting OD_{600} 0.05
429 in 250 ml Erlenmeyer flasks. Cultures were grown at 37°C 180 rpm in a water bath. OD_{600} was
430 monitored every 30 minutes. The average and standard deviation of three biological replicates
431 were calculated.

432 Heat shock survival

433 Cultures were inoculated in 25 ml LB medium to OD_{600} 0.05 and incubated in a water bath at
434 37°C 180 rpm. At OD_{600} 0.3 – 0.4, the cultures were exposed to a heat shock at 54°C for 2
435 hours, and samples for viability measurement were obtained every 30 minutes. Viability was
436 measured by spotting 4 µl of 1:10 serial dilutions in PBS of each sample on LB agar. The plates
437 were incubated overnight at 30°C, and the colony-forming units (CFU) were counted. The

438 CFU/ml was calculated for each sample, and relative viability was determined using samples
439 before heat shock as a reference.

440 Isolation of protein aggregates

441 Twenty-five ml of culture were harvested before and 15 minutes after heat shock at 54°C by
442 centrifugation for 5 minutes at 10,000 rpm. The pellets were washed once with buffer A (100
443 mM HEPES pH 8.0, 150 mM NaCl) and lysed by bead-beating in buffer B (100 mM HEPES
444 pH 8.0, 150 mM NaCl, cOmplete EDTA-free protease inhibitor) using 0.1 mm glass beads.
445 Afterwards, samples were centrifuged at 1000 x *g* for 2 minutes to obtain the cell extract. The
446 soluble fraction was separated from protein aggregates by centrifugation for 15 minutes at
447 11,000 x *g* at 4°C. To remove membrane proteins, the aggregates were resuspended in buffer
448 B containing 1% Triton X-100 and incubated for 1 hour at 4°C. Protein aggregates were
449 recovered by centrifugation at 11,000 x *g*, 4°C for 15 minutes and resuspended and incubated
450 as described above. Protein aggregates were washed again with buffer B + 0.5% Triton X-
451 100, and the detergent was removed in a final wash using buffer B. Pellets containing protein
452 aggregates were resuspended in buffer B + 2% SDS by boiling for 5 minutes at 95°C. Protein
453 concentration was measured using the Rapid Gold BCA Protein-Assay-Kit (Pierce™, A53225).
454 The percentage of aggregated protein was calculated to the total protein content in the cell
455 extract.

456 Spot test

457 Overnight cultures were diluted 1:1000 in LB medium without antibiotics and incubated at 37°C
458 180 rpm for 7-8 hours. The cultures were diluted to OD_{600} 1 in fresh LB medium in a 96-well
459 plate. Seven serial 1:10 dilutions were prepared in 1x PBS. Four µl of each dilution was spotted
460 on LB agar containing different stressors (concentration indicated in the figures). Plates were
461 freshly prepared before use.

462 RNA purification

463 Samples for RNA purification were collected at the indicated time points: exponential phase
464 (OD_{600} ~ 0.3), late exponential phase (OD_{600} ~ 1) and transition phase (100 minutes after late
465 exponential phase). Rifampicin was added to a final concentration of 100 µg/ml for 10 minutes.

466 Samples were harvested by mixing with the same volume of cold 1:1 acetone:ethanol and
467 centrifugated at 9,000 rpm for 5 minutes, 4°C. RNA purification was performed according to
468 Ref.[27] with slight modifications: The pellet was washed twice in 1 ml TE-sucrose buffer (50 mM
469 Tris-HCl pH 8.0, 10 mM EDTA, 25% sucrose) and centrifugated at 10,000 rpm for 5 minutes,
470 4°C. Cells were resuspended in 130 µl lysis buffer (20 mM Tris-HCl pH 8.0, 50 mM EDTA, 20
471 % sucrose) supplemented with 3.2 mg/ml lysozyme and incubated on ice for 5 minutes. Two
472 hundred µl of lysis executioner (2% SDS, 1 mg/ml Proteinase K) were added to the samples

473 and incubated at 95°C for 1.5 minutes. Samples were mixed with 1 ml of TRIzol (Ambion) and
474 incubated at room temperature. After 5 minutes, 250 µl chloroform was added to each sample
475 and mixed by vortexing. After 10 minutes at room temperature, the samples were centrifuged
476 for 10 minutes at 11,000 rpm. The RNA was isopropanol-precipitated at -20°C overnight. RNA
477 was pelleted at 11,000 rpm for 20 minutes at 4°C, washed with 1 ml 70% ethanol followed by
478 another centrifugation at 13,000 rpm for 10 minutes at 4°C. The pellet was air-dried and
479 resuspended in 50 µl nuclease-free water.

480 ISCP RNA sequencing

481 RNA sequencing was performed as previously described[70]. In brief, total RNA was treated with
482 TURBO DNase (Ambion, AM2238), depleted of ribosomal RNA using the riboPOOL rRNA
483 depletion kit for *B. subtilis* (siTOOLS; two reactions with 4.5 µg each) and purified using the
484 RNA Clean & Concentrator-5 kit (RCC-5; Zymo Research). RNA 5' triphosphates were
485 converted to monophosphates using RppH (NEB), and RNA was recovered using
486 phenol:chloroform:isoamyl alcohol extraction followed by ethanol precipitation. RNA ends were
487 repaired using T4 Polynucleotide Kinase (Thermo Scientific), before RNA was purified using
488 the RCC-5 kit and fragmented using an M220 Focused-ultrasonicator (Covaris) as described
489 by the manufacturer but with a treatment time of 100 s (microTUBE AFA Fiber Snap-Cap). After
490 purification using the RCC-5 kit, sequencing libraries were prepared from the recovered RNA
491 using the NEXTflex Small RNA-Seq Kit v3 (Bioo Scientific) according to the manufacturer's
492 protocol (including step G). Libraries were purified as described in step I of the NEXTflex Rapid
493 Directional qRNA-Seq Kit (Bioo Scientific) using Agencourt AMPure XP Beads (Beckman
494 Coulter; 0.9x bead-to-sample ratio). Sequencing was performed on an Illumina NovaSeq 6000
495 in paired-end mode with a read length of 100 bp at the Sequencing Core Facility of the Max
496 Planck Institute for Molecular Genetics (Berlin, Germany).

497 Processing of RNA sequencing data

498 FastQC (v0.11.5) was used to assess the quality of the data. Reads were filtered with a
499 minimum quality score of 10 and a length of at least 18 nt, cleaned from adapter sequences
500 using Cutadapt (v3.5)[71], and mapped against the *B. subtilis* reference genome (NC_000964.3)
501 using STAR (v2.7.10a_alpha_220314)[72] in 'random best' and 'end to end' modes. Resulting
502 BAM files were sorted and indexed with Samtools (v1.9)[73], and PCR duplication artefacts were
503 removed using UMI Tools (v1.1.0)[74]. Gene counts of annotated RefSeq genes were
504 determined with featureCounts (v2.0.3)[75] and differentially expressed genes (DEG) were
505 calculated with three replicates per condition and time point using DESeq2 (v1.24.0)[76]. *p*-
506 values were corrected for multiple testing using the Benjamini-Hochberg method[69]. To call
507 DEGs, a threshold of adjusted *p*-value < 0.05 and absolute log2 fold change > 1 was used.

508 Genome coverage profiles (total, 5' and 3' ends) were generated using a custom script utilizing
509 the HTSeq library (v2.0.2)[77]. We performed the aforementioned analysis steps using a
510 customized pipeline implemented in Snakemake (v7.14.0)[78].

511 Identification of Y complex cleavage sites

512 The Y-complex-dependent cleavage positions were identified following the previously
513 published procedure[70]. In brief, the genome coverage data was prefiltered with a count per
514 million (cpm) value ≥0.05, and only the RNA ends displaying a cpm ≥ 5 were further analyzed.
515 We carried out differential expression analysis of normalized 5′ and 3′ read ends by comparing
516 WT vs. Δ*ymcA* at the late exponential and transition phase. Y-complex-dependent ends were
517 identified using edgeR (v3.28.0)[79] with absolute log2 fold change ≥ 1 and FDR < 0.05, and kept
518 only if present in both comparisons. These results were further filtered with additional
519 parameters, i.e., the "proportion of ends (cleavage ratio)" and the "ratio of WT and Δ*ymcA*
520 proportion of ends" as was previously described[70]. Moreover, to reduce the potential set of
521 false positive processing sites even further, we applied an additional cut-off on the "proportion
522 of ends" parameter, i.e., we kept only processing sites with a cleavage ratio of the reference
523 strain (WT) ≥ 95%-percentile of the cleavage ratio of the mutant strain.

524 Impact of processing sites on transcript and operon expression

525 To examine the impact of cleavage sites on transcript and operon expression, as well as other
526 genomic features such as untranslated regions (UTRs) and regulatory elements, we calculated
527 transcript per million (TPM) values from variance-stabilized data for each annotated RefSeq
528 gene (transcript level) and for each operon as defined in the BSGatlas (v1.1)[80] using the
529 DESeq2 package and a custom Python script. Furthermore, all Y-complex-dependent
530 cleavage sites were mapped to various genomic features, including coding regions, UTRs,
531 terminator regions, and riboswitches, as defined in the BSGatlas[80] (**Table S2**).

532 Processing site sequence logo

533 The sequence logos were generated with Logomaker (v0.8)[81], specifically for 5' and 3' end U-
534 type cleavage sites. For this, we extracted 30 nt sequences centered at the cleavage site and
535 calculated the logos with a GC content of 43.5%.

536 RNA secondary structure prediction

537 The RNA structure surrounding Y-complex-dependent cleavage sites was estimated by
538 calculating the MFE (ΔG in kcal/mol) utilizing RNAfold (v2.6.4)[82]. This analysis employed a
539 sliding window approach with 50 nt sequences, focusing on a 200 nt region centered around
540 the position of interest. The average MFE at each nucleotide was then calculated. To calculate
541 and visualize the background folding energy, we randomly draw potential processing sites from

542 the genome determined with the corresponding 5' or 3' end motif and calculate the average
543 MFE at each nucleotide as described above. Potential processing sites were drawn 50 times
544 independently.

545 Overrepresentation analysis

546 Annotations of operons were obtained from BSGatlas[80] and gene categories from Subtiwiki
547 (24 July 2023)[83]. The overrepresentation analysis was performed using the R statistical
548 computing language (v.4.2.2) and the Bioconductor package Category (v.2.64.0).

549 Northern blot

550 Biotinylated RNA probes were prepared using the HighYield T7 Biotin11 RNA Labeling Kit
551 (UTP-based) (Jena Bioscience, RNT-101-BIOX) from PCR amplified fragments containing the
552 promoter for the T7 RNA polymerase (**Table S11**). Probes were purified using the Monarch®
553 Spin RNA Cleanup Kit (NEB, T2040) according to the manufacturer's instructions. Probes were
554 designed taking into consideration the predicted cleavage sites.

555 One and a half µg of total RNA was separated on denaturing agarose gels (1% agarose,
556 20 mM MOPS, 5 mM NaOAc, 1 mM EDTA, 6.6% formaldehyde, pH 7.0) in 1x AGE-NB
557 Running Buffer (20 mM MOPS, 5 mM NaOAc, 1 mM EDTA, 0.74% formaldehyde, pH 7.0).
558 The gel was washed 3 times with milli-Q water and once with 10x SSC buffer, and the
559 nitrocellulose membrane was washed once with milli-Q water and once with 10x SSC. The
560 RNA was transferred using a vacuum blotter at 300 mbar covered with 10x SSC for 1.5 hours.
561 After transfer, the membrane was washed for 2 minutes with 6x SSC, once with water, and
562 dried and crosslinked at 254 nm 0.12 J twice. The membrane was developed with methylene
563 blue, and the staining was removed by washing with 0.2x SSC containing 1% SDS, followed
564 by washing with milli-Q water. The hybridization of 16S or 23S rRNA probes was performed
565 using the North2South Chemiluminescent Hybridization and Detection Kit (Thermo) and
566 North2South Hybridization Stringency Wash Buffer (2X) according to the manufacturer's
567 instructions. Blots were developed in a Vilber imaging system.

568 RT-qPCR

569 Twenty µg of total RNA were treated with TURBO DNase (Ambion, AM2238) and purified using
570 the Monarch® Spin RNA Cleanup Kit (NEB, T2040). Subsequently, cDNA was prepared using
571 the LunaScript RT Mastermix (NEB, E3025) and 2.5 µg of DNase-treated RNA as input.
572 Quantitative PCR was performed using the Luna Universal qPCR Master Mix (NEB, M3003)
573 in a QuantStudio 5 Real-Time PCR System (Applied Biosystems). To calculate changes in *gfp*
574 transcription, samples from the late exponential and transition phases were compared to those

575 from the exponential phase, with *pcp* serving as a reference gene using the Pfaffl method[84].
576 Primers used for RT-qPCR are listed in **Table S11**.

577 Ribosome sedimentation in sucrose gradients

578 Cultures of WT and Δ*ymcA* were grown until the exponential phase (OD_{600} ~ 0.3), late
579 exponential (OD_{600} ~ 1), and transition phase (100 minutes after the late exponential phase).
580 Chloramphenicol was added at a concentration of 100 µg/ml 2 minutes prior to sample
581 collection. Fifty ml of culture were pelleted at 4,500 rpm for 10 minutes at room temperature.
582 Pellets were transferred to ice and resuspended in 2 ml of lysis buffer (20 mM Tris-HCl pH 8.0,
583 100 mM NH_4Cl, 10 mM $MgCl_2$, 0.4% Triton X-100, 0.4% NP-40, 1 mM chloramphenicol, 100
584 U/µl DNase I), and flash-frozen. Cells were lysed under cryogenic conditions using 5 cycles of
585 mix-milling at 30 Hz for 1 minute. Lysates (240 µg RNA) were laid over a 10-50% sucrose
586 gradient in 20 mM Tris-HCl pH 8.0, 100 mM NH_4Cl, 10 mM $MgCl_2$, 0.5 mM DTT and resolved
587 at 35,000 rpm for 3 hours at 4°C. Gradients were analyzed using a piston fractionator (Biocomp
588 instruments), and absorbance at 260 and 280 nm was monitored.

589 Sample preparation for MS-based proteomics

590 Samples were collected at the indicated time points: late exponential phase (OD_{600} ~ 1) and
591 transition phase (100 minutes after the late exponential phase). For the proteomic changes
592 during heat shock, cultures were grown at 37°C until OD_{600} ~ 0.3 and shifted to 54°C. Samples
593 were collected at 0, 15, 30, and 60 minutes after heat shock. Ten ml of culture were collected
594 by centrifugation at 4,500 rpm for 10 minutes, and the pellet was stored at -80°C until further
595 processing.

596 Cell pellets were resuspended in 1 ml of cold PBS and centrifuged at 13,000 rpm for 5 minutes
597 at 4°C. The pellet was washed once more with PBS, resuspended in 150 µL of lysis buffer
598 (100 mM HEPES pH 8.0, 2% SDS, 20 mM TCEP, 60 mM CAA), and lysed using bead beating.
599 Cell debris was discarded by centrifuging at 13,000 rpm for 5 minutes at 4°C. The supernatant
600 was boiled at 95°C for 5 minutes, cooled down to room temperature, and the protein
601 concentration was estimated using the Rapid Gold BCA protein assay kit (Pierce). Samples
602 were flash-frozen in liquid nitrogen and stored at -80°C until further processing.

603 All samples were subjected to SP3 sample preparation[85] on an Agilent BRAVO liquid handling
604 robot. Ten µg of a 1:1 mixture of hydrophilic and hydrophobic carboxyl-coated paramagnetic
605 beads (SeraMag, #24152105050250 and #44152105050250, GE Healtcare) were added for
606 each µg of protein. Protein binding was induced by the addition of acetonitrile to a final
607 concentration of 50% (v/v). Samples were incubated at room temperature for 10 minutes. The
608 tubes were placed on a magnetic rack, and beads were allowed to settle for 3 minutes. The
609 supernatant was discarded, and beads were rinsed three times with 200 µL of 80% ethanol

610 without removing the tubes from the rack. Beads were resuspended in digestion buffer
611 containing 50 mM triethylammonium bicarbonate and both Trypsin (Serva) and Lys-C (Wako)
612 in a 1:50 enzyme-to-protein ratio. Protein digestion was performed for 14 hours at 37°C in a
613 PCR cycler. Afterward, the supernatant was recovered and dried down in a vacuum
614 concentrator.

615 Proteomics using Mass spectrometry

616 All samples obtained during the late exponential and transition phase were analyzed on an
617 Orbitrap Exploris (Thermo Scientific) equipped with a FAIMS Pro device and coupled to a 3000
618 RSLC nano UPLC (Thermo Scientific). Samples were loaded on a PepMap trap cartridge (300
619 µm i.d. x 5 mm, C18, Thermo) with 2% acetonitrile and 0.1% TFA at a flow rate of 20 µl/min.
620 Peptides were separated over a 50 cm analytical column (Picofrit, 360 µm O.D., 75 µm I.D.,
621 10 µm tip opening, non-coated, New Objective) that was packed in-house with Poroshell 120
622 EC-C18, 2.7 µm (Agilent). Solvent A consists of 0.1% formic acid in water. Elution was carried
623 out at a constant flow rate of 300 nl/min using a 60-minute method: 8-30% solvent B (0.1%
624 formic acid in 80% acetonitrile) within 23 minutes, 30-45% solvent B within 3 minutes, 45-98%
625 buffer B within 0.5 minutes, followed by column washing and equilibration. Data acquisition on
626 the Orbitrap Exploris was carried out using a data-dependent acquisition (**DDA**) method in
627 positive ion mode. MS survey scans were acquired from 375-1500 m/z in profile mode at a
628 resolution of 60,000. AGC target was set to 200% at a maximum injection time of 25 ms.
629 Peptides with charge states 2-6 were isolated within a window of 1.2 m/z and subjected to
630 HCD fragmentation at a normalized collision energy of 27%. The MS2 AGC target was set to
631 200%, allowing a maximum injection time of 22 ms. Product ions were detected in the Orbitrap
632 at a resolution of 15,000. Precursors were dynamically excluded for 20 s. The cycle time was
633 set to 1 s for each of the two FAIMS voltages of −45 and −65 V.

634 LC-MS/MS analysis of the heat shock samples was performed on an Ultimate 3000 UPLC
635 coupled to a Lumos hybrid mass spectrometer (Thermo Scientific). Peptides were loaded onto
636 a PepMap trap cartridge (300 µm i.d. x 5 mm, C18, Thermo) with 2% acetonitrile and 0.1%
637 TFA at a 20 µl/min flow rate. Peptides were separated over a 50 cm analytical column (Picofrit,
638 360 µm O.D., 75 µm I.D., 10 µm tip opening, non-coated, New Objective) that was packed in-
639 house with Poroshell 120 EC-C18, 2.7 µm (Agilent). Solvent A consists of 0.1% formic acid in
640 water. Elution was carried out at a constant flow rate of 250 nl/min using a 60-minute method:
641 8-30% solvent B (0.1% formic acid in 80% acetonitrile) within 23 minutes, 30-45% solvent B
642 within 3 minutes, 45-98% buffer B within 0.5 minutes, followed by column washing and
643 equilibration.

644 The mass spectrometer was operated in data-independent acquisition (**DIA**) and positive
645 ionization mode. MS1 full scans (375–1500 m/z) were acquired with a resolution of 60,000, a

646 normalized automatic gain control target value of 120%, and a maximum injection time set to
647 55 ms. Peptide fragmentation was performed using higher energy collision-induced
648 dissociation and a normalized collision energy of 30%. MS2 spectra were acquired with a
649 resolution of 30,000 (first mass 100 m/z) with 8 m/z DIA windows between 400 and 1200 m/z.
650 A normalized automatic gain control target value of 100%, and a maximum injection time of
651 54 ms.

652 Proteomics data analysis

653 For samples at the late exponential and transition phase, Raw files were processed with
654 MSFragger v3.5 using the default settings. Briefly, peak lists were extracted from raw files and
655 searched using a Uniprot *Bacillus subtilis* database (v220530, taxonomy ID 224308) and a
656 database containing sequences of common contaminants and decoys. Trypsin/P was set as
657 enzyme specificity, allowing a maximum of two missed cleavages. Peptide matches were
658 filtered to 1% FDR using PeptideProphet and Philosopher (v4.4.0).

659 For samples during heat shock, DIA-NN (DIA-NN v1.8.1) was employed for DIA data analysis.
660 The main DIA-NN report, "report.txt", was used for all calculations. Fasta file
661 (Bacillus_subtilis_Strain168_UP000001570.fasta) was digested with a maximum of one
662 missed cleavage. Peptide length was restricted from 7 to 30 peptides, and the precursor m/z
663 range was set from 300 to 1800. N-terminal methionine excision was enabled. Cysteine
664 carbamidomethylation was selected as a fixed modification, and methionine oxidation and N-
665 terminal acetylation as variable modifications. The maximum number of variable modifications
666 was set to two. All other parameters were at default settings, including the 1% precursor FDR
667 and enabled match between runs (MBR). The main DIA-NN report, "report.pg_matrix.tsv," was
668 used for all calculations.

669 The R statistical computing language was used for data processing (v4.4.1). The main
670 comparison of WT, Δ*ymcA*, (p)ppGpp^{0,} and (p)ppGpp^{0} Δ*ymcA* mutants was based on samples
671 from data-dependent acquisition (DDA) experiments. Raw peptide intensity values from label-
672 free quantitation were imported as tabular output from MSFragger. The MSstats package
673 (v4.12.1)[86] was used to convert raw intensities to an MSstats experiment. In this process,
674 peptide quantification data was $\log_2$-transformed, median-normalized, and summarized to
675 protein abundance. All features mapping to a protein were used for quantification, Tukey's
676 median polish was used as a summarization strategy, and missing values were imputed using
677 MSstats' default strategy. Feature abundance and inferred protein quantity were visually
678 inspected using profile plots. Experimental groups were compared using MSstats'
679 *groupComparison* function, and the similarity of conditions and replicates was inspected using
680 principal component analysis (PCA, function *prcomp*). For annotation, protein-related
681 information was fetched from Uniprot using the Uniprot REST API (14 June 2024). In addition

682 to the DDA experiments, a time series of WT and Δ*ymcA* mutants was obtained using data-
683 independent acquisition (DIA) proteomics. To quantify relative changes, the $\log_2$ fold change
684 of each time point was calculated using the zero time point as a reference. To quantify absolute
685 protein abundance for the ribosomal proteome sector, the coarse-graining strategy was used
686 as in Ref.[87,88]. Briefly, two protein sectors (groups) were created containing all annotated
687 proteins of ribosomal subunits. Raw MS1 intensities for all proteins of the respective group and
688 time points were summed up and divided by the total sum of protein intensities, yielding the
689 protein mass fraction per sector.

690 **Data availability**

691 Amplicon-seq and RNA-seq raw reads have been deposited at the European Nucleotide
692 Archive (ENA) under accession number PRJEB90661. Raw proteomic data have been
693 deposited at the PRIDE database under the accession number PXD065465 for DDA
694 proteomics of late exponential and transition phase samples (Reviewer access in PRIDE
695 (https://www.ebi.ac.uk/pride/login), Token: ijwEKpkL6sTq). The DIA proteomics raw data from
696 the heat shock experiment can be accessed using the accession number PXD065462
697 (Reviewer access in PRIDE, Token: 8IRshuji8qRS).

698 **Author contributions**

699 K.T., K.D., and F.A.C.; Conceptualization. K.D., F.A.C., K.T., R.A.-B., T.F.W., and K.A.:
700 Methodology. F.A.C., K.D., K.S., V.S., K.H., and F.K.: Investigation. K.D., F.A.C., R.A.-B., M.J.,
701 K.A., S.R., and K.T.: Formal analysis. F.A.C., K.D., R.A.-B., M.J.: Visualization. F.A.C., K.D.,
702 and K.T.: Writing – Original Draft. K.T. and E.C.: Funding acquisition. All authors: Writing –
703 Review & Editing.

704 **Acknowledgments**

705 We thank Gert Bange (Philipps-Universität Marburg) and Rainer Nikolay (Max Planck Institute
706 for Molecular Genetics) for critically reading the manuscript and providing valuable feedback.
707 This work was funded by the Deutsche Forschungsgemeinschaft (Tu106/8, SPP1879 for K.D.
708 and K.T., Leibniz Prize for E.C.) and the Max Planck Society (for E.C. and K.T.).

709

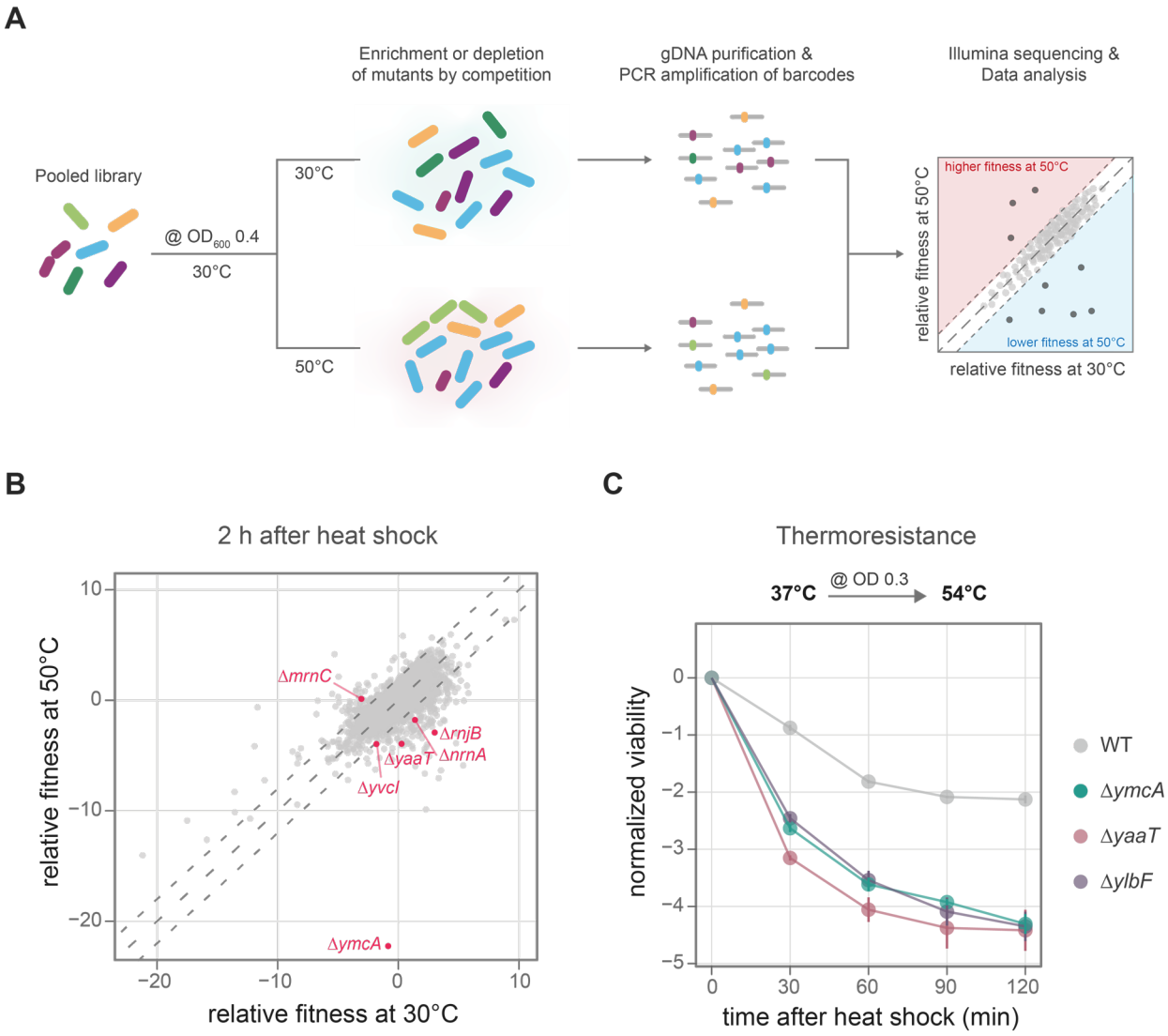

Figure 1. Genetic screening for genes involved in the heat shock response. A) Genetic screening experiment: the pooled library of deletion mutants (BKE) was grown at 30°C; when it reached an OD_{600nm} of 0.4, one fraction was exposed to 50°C while the other was maintained at 30°C. Genomic DNA (gDNA) was extracted from the library, and barcodes were amplified and sequenced using Next-Generation Sequencing. The fitness of each mutant at the mentioned temperatures and time points was calculated using BEANcounter. **B**) Relative fitness of each deletion mutant at 50°C (*y*-axis) and 30°C (*x*-axis) two hours post-temperature shift. Each point represents a deletion mutant, with mutants lacking RNase-related genes highlighted in magenta. The dotted lines indicate the range in which the relative fitness between the conditions differed by less than 2. Data represent the average of three biological replicates. A negative relative fitness value means that the abundance of the deletion mutant, compared to the rest of the population, was negatively affected by the treatment, while a positive value means an increased abundance in this condition. **C)** Changes in the viability (log_{10}CFU/ml) of WT and *ymcA, ylbF,* and *yaaT* deletion mutants to a severe heat shock at 54°C. Values were normalized to the viability at timepoint 0 min. The data represents the average ± standard error of three biological replicates.

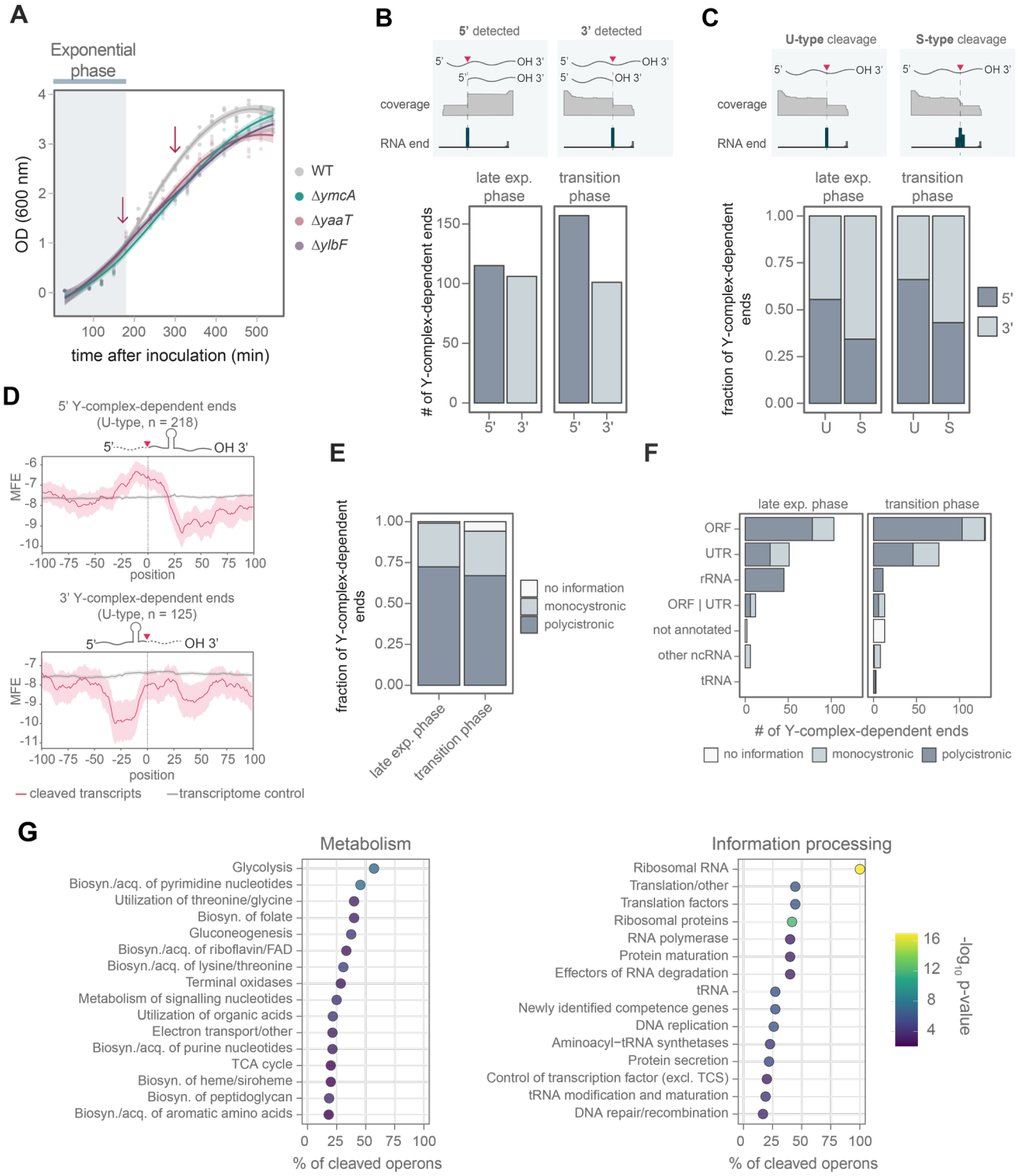

Figure 2. Identification of Y-complex-dependent cleavages at late exponential and transition phase. A) Growth curves of WT, *ymcA*, *ylbF*, and *yaaT* deletion mutants in LB at 37°C. The blue bar marks the exponential phase. Arrows indicate sample collection for the ISCP method at the late exponential and transition phases. Three biological replicates are displayed with a smooth curve regression. **B)** Number of RNA 3' or 5' ends identified at the two growth phases. **C)** Fraction of identified 3' or 5' ends displaying U-type (unique) or S-type (stepped) profiles. **D)** Minimum free energy (MFE) was calculated on 50 nt windows for RNAs cleaved by the Y-complex with U-type ends (in magenta). Transcripts that share the same cleavage motif but are not processed were used as a control (in gray). rRNA genes were excluded from the analysis since they are highly structured. **E)** Fractions of ends identified in genes transcribed in polycistronic or monocistronic RNA. **F)** Count of RNA features where

Y-complex-dependent ends are detected at either growth phase. Annotations were obtained from BSGatlas[80]. **G)** Overrepresentation analysis of pathways whose transcripts are cleaved by the Y-complex during the late exponential phase. Operons were assigned to be involved in a pathway if they code for one gene participating in such a pathway. As genes in the same operon can have different functions, transcripts may be linked to multiple roles. Pathway annotations were retrieved from SubtiWiki[83]. The color indicates the statistical significance of the enrichment. Biosyn = biosynthesis, acq = acquisition, excl TCS = excluding two-component systems.

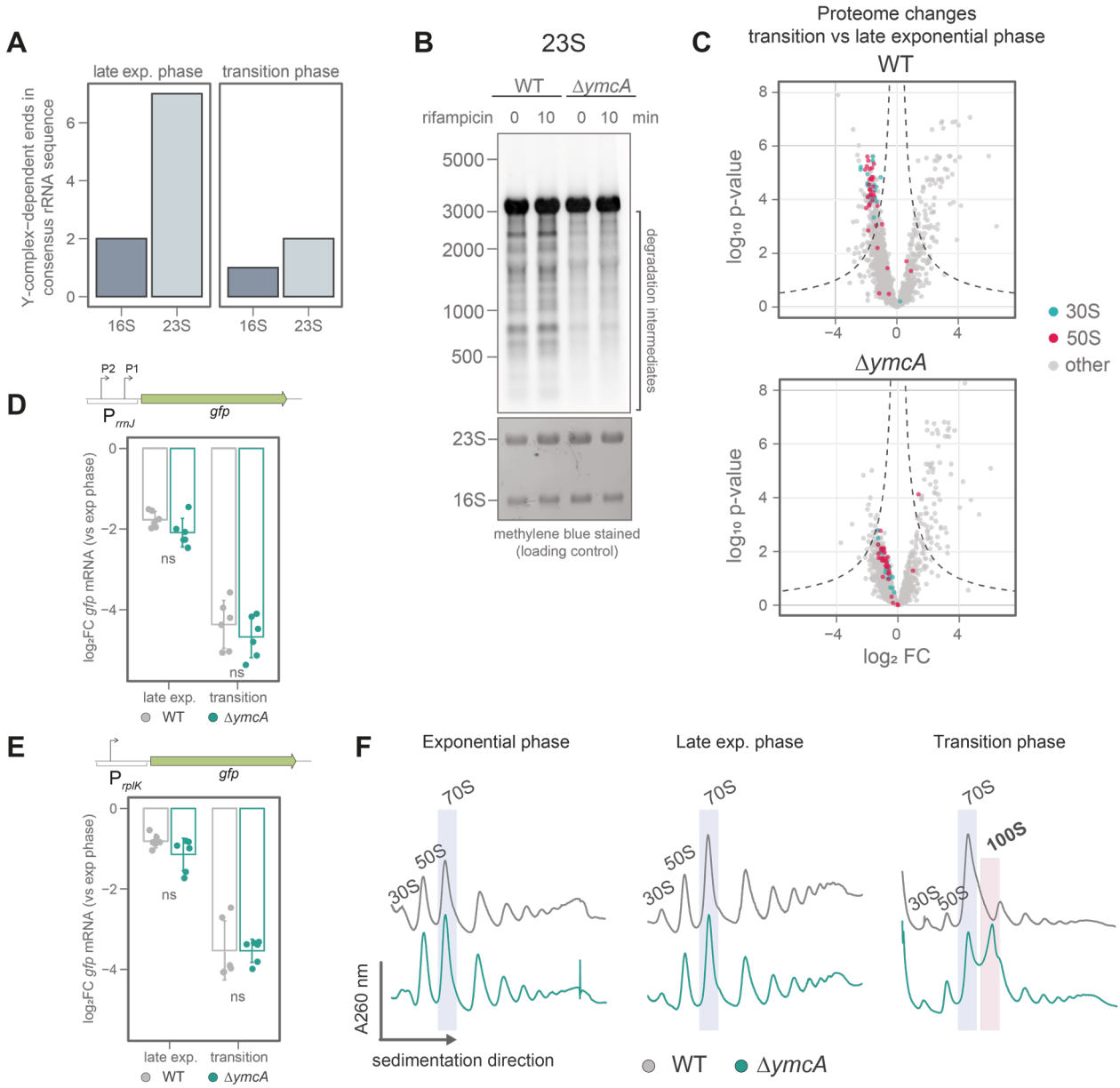

Figure 3. The Y-complex controls ribosome levels by initiating rRNA degradation. A) Number of cleavages detected by ISCP in *B. subtilis* rRNA during the late exponential and transition phase. **B)** Northern blot against 23S of WT and Δ*ymcA* cells at the late exponential phase, before and after treatment with 100 µg/ml rifampicin to stop transcription. The methylene blue-stained membrane is shown as a loading control. This image is representative of three biological replicates. **C)** Volcano plot of protein quantification of WT and Δ*ymcA* strains comparing transition to late exponential phase. The proteins composing the small (30S) and major (50S) ribosome subunits are highlighted in cyan and magenta, respectively. The data shows the average of four biological replicates. Activity of the promoter controlling **D)** *rrnJ* (rRNA) or **E)** the *rplK* (r-protein) transcription at late exponential and transition phase compared to the exponential phase in WT and Δ*ymcA*. The promoters were cloned controlling *gfp* transcription, which was measured using RT-qPCR. The *pcp* transcript was used as a reference. Individual values and the average ± standard deviation of three biological replicates and two technical replicates are shown. The statistical significance was tested using student's *t*-test. ns: *p*-value > 0.05. **F)** Ribosome sedimentation profile in 10-50% sucrose gradients of WT and Δ*ymcA* in exponential, late exponential, and transition phases. The 70S and 100S ribosomes are highlighted with a blue or red box, respectively. The data is representative of three biological replicates.

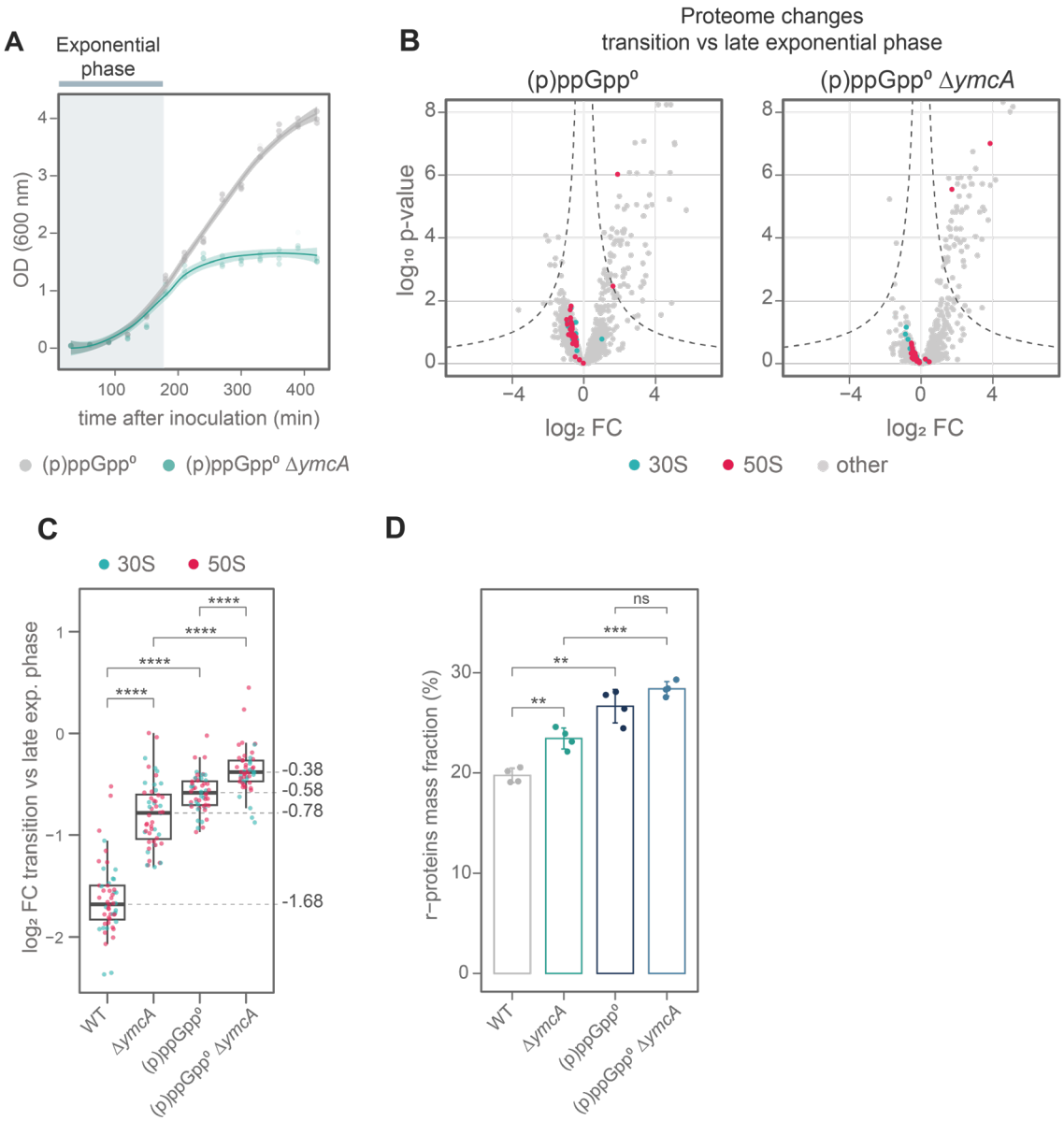

Figure 4. The alarmones (p)ppGpp and the Y-complex are important for controlling ribosome levels. A) Growth curve of (p)ppGpp^0 and (p)ppGpp^0 Δ*ymcA* strains in LB at 37°C. The blue bar marks the exponential phase. Three biological replicates are displayed with a smooth curve regression. **B)** Volcano plot of proteomic changes of (p)ppGpp^0 and (p)ppGpp^0 Δ*ymcA* cultures comparing transition to exponential phase. The proteins composing the small (30S) and major (50S) ribosome subunits are highlighted in cyan and magenta, respectively. The data shows the average of four biological replicates. **C)** Comparison of r-proteins downregulation in WT, Δ*ymcA,* (p)ppGpp^{0,} and (p)ppGpp^0 Δ*ymcA* during the transition phase compared to the late exponential phase. The boxplot represents the interquartile range (IQR) and the median in the center. Whiskers show the variability outside quartile 1 (Q1) and Q3 and were calculated as Q1-1.5*IQR and Q5+1.5*IQR, respectively. Proteins are highlighted like in **B**. Alternative r-proteins were excluded from the analysis. The statistical significance was tested using paired Wilcoxon test. ****: *p*-value ≤ 0.0001. **D)** Proteome fraction (in %) of r-proteins mass, measured by mass spectrometry. The r-protein mass fraction was calculated for the indicated strains. Individual values and the average ± standard deviation of three biological replicates are shown. The statistical significance was tested using student's *t*-test. ns: *p*-value > 0.05, **: *p*-value ≤ 0.01, ***: *p*-value ≤ 0.001.

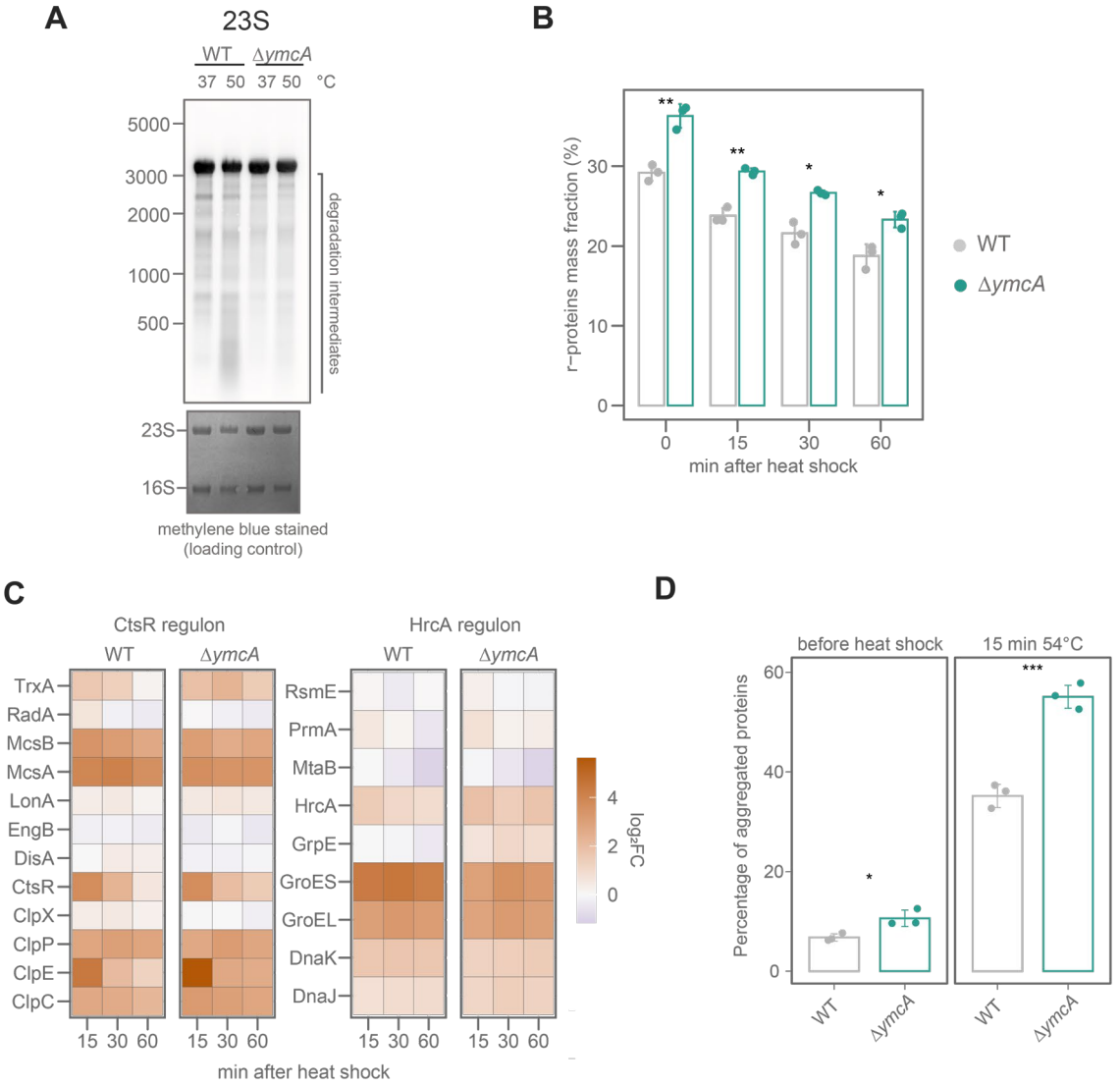

Figure 5. Control of ribosome levels and protein homeostasis in *ymcA* mutant during heat shock. **A)** Northern blot against 23S of WT and Δ*ymcA* cells at exponential phase before or after a heat shock. The methylene blue-stained membrane is shown as a loading control. This image is representative of three biological replicates. **B)** Proteome fraction (in %) of r-proteins mass, measured by mass spectrometry. Individual values and the average ± standard deviation of three biological replicates are shown. The statistical significance was tested using student's *t*-test. *: *p*-value ≤ 0.05, **: *p*-value ≤ 0.01. **C)** Induction of CtsR and HrcA regulons after heat shock (50°C) in WT and Δ*ymcA*. Proteins were measured by mass spectrometry. The color bar shows the $\log_2$ fold change compared to the control before heat shock. **D)** Percentage of aggregated proteins before and after a 15 min heat shock at 54°C in WT and Δ*ymcA*. Individual values and the average ± standard deviation of three biological replicates are shown. The statistical difference was tested using student's *t*-test. *: *p*-value ≤ 0.05, **: *p*-value ≤ 0.01, ***: *p*-value ≤ 0.001.

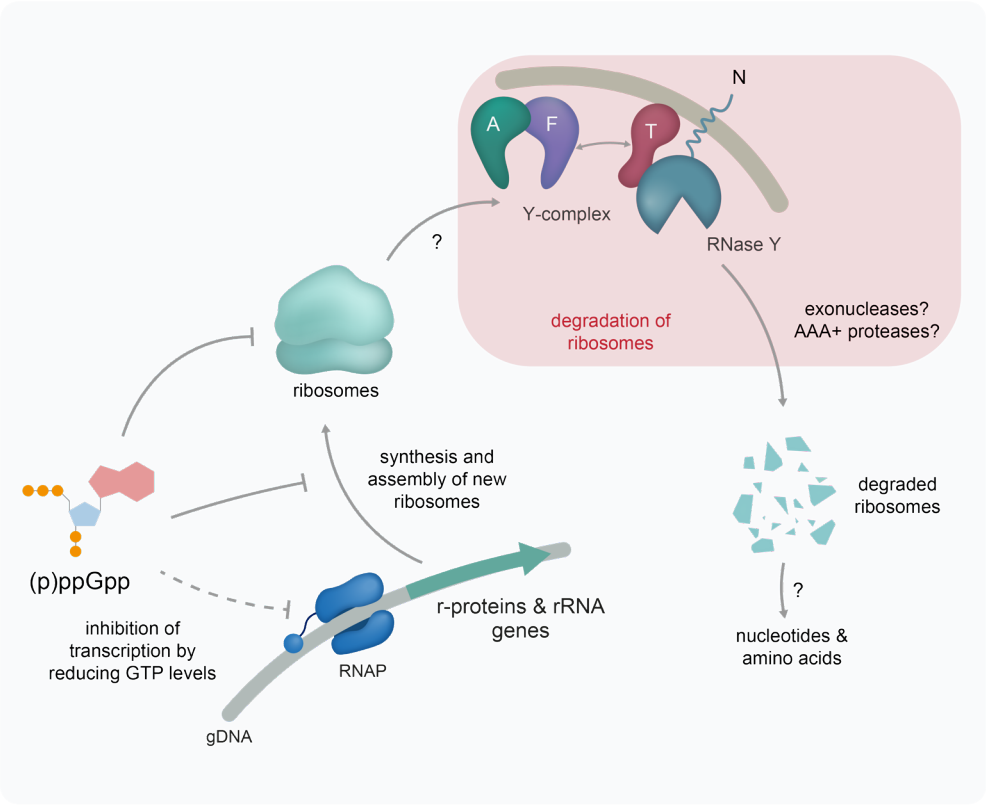

794

795 **Figure 6. Control of ribosome levels by (p)ppGpp and the Y-complex.** The alarmone (p)ppGpp
796 reduces the biogenesis of new ribosomes by indirectly inhibiting the transcription of rRNA and r-proteins
797 mRNA. (p)ppGpp inhibits GTPases that are involved in new ribosome assembly. Additionally, (p)ppGpp
798 reduces translation by binding to specific GTPases. The Y-complex can initiate the degradation of
799 ribosomes, which need to be transported to the membrane by unknown mechanisms. Exonucleases
800 and AAA+ protease complexes might assist in ribosome degradation for the complete degradation of
801 rRNA and r-proteins, which could partially replenish the nucleotide and amino acid pools during
802 starvation.

803

804 **References**

805 1. Hecker, M., Schumann, W., and Völker, U. (1996). Heat-shock and general stress response in
806 *Bacillus subtilis*. Mol. Microbiol. *19*, 417–428. https://doi.org/10.1046/j.1365-2958.1996.396932.x.

807 2. Mogk, A., Homuth, G., Scholz, C., Kim, L., Schmid, F.X., and Schumann, W. (1997). The GroE
808 chaperonin machine is a major modulator of the CIRCE heat shock regulon of *Bacillus subtilis*.
809 EMBO J. *16*, 4579–4590. https://doi.org/10.1093/emboj/16.15.4579.

810 3. Krüger, E., and Hecker, M. (1998). The first gene of the *Bacillus subtilis clpC* operon, *ctsR*,
811 encodes a negative regulator of its own operon and other Class III heat shock genes. J. Bacteriol.
812 *180*, 6681–6688. https://doi.org/10.1128/jb.180.24.6681-6688.1998.

813 4. Elsholz, A.K.W., Michalik, S., Zühlke, D., Hecker, M., and Gerth, U. (2010). CtsR, the Gram-
814 positive master regulator of protein quality control, feels the heat. EMBO J. *29*, 3621–3629.
815 https://doi.org/10.1038/emboj.2010.228.

816 5. Krüger, E., Witt, E., Ohlmeier, S., Hanschke, R., and Hecker, M. (2000). The Clp proteases of
817 *Bacillus subtilis* are directly involved in degradation of misfolded proteins. J. Bacteriol. *182*, 3259–
818 3265. https://doi.org/10.1128/jb.182.11.3259-3265.2000.

819 6. Alver, R., Hantke, I., Cornejo, F.A., Gunka, K., Rämisch, S., Molière, N., Charpentier, E., and
820 Turgay, K. (2023). The control of protein arginine phosphorylation facilitates proteostasis by an
821 AAA+ chaperone protease system. Preprint at bioRxiv, https://doi.org/10.1101/2022.09.15.508104
822 https://doi.org/10.1101/2022.09.15.508104.

823 7. Schäfer, H., Beckert, B., Frese, C.K., Steinchen, W., Nuss, A.M., Beckstette, M., Hantke, I.,
824 Driller, K., Sudzinová, P., Krásný, L., et al. (2020). The alarmones (p)ppGpp are part of the heat
825 shock response of *Bacillus subtilis*. PLOS Genet. *16*, e1008275.
826 https://doi.org/10.1371/journal.pgen.1008275.

827 8. Clay, K.J., Yang, Y., Clark, C., and Petrascheck, M. (2023). Proteostasis is differentially
828 modulated by inhibition of translation initiation or elongation. eLife *12*, e76465.
829 https://doi.org/10.7554/eLife.76465.

830 9. Cherkasov, V., Hofmann, S., Druffel-Augustin, S., Mogk, A., Tyedmers, J., Stoecklin, G., and
831 Bukau, B. (2013). Coordination of translational control and protein homeostasis during severe
832 heat stress. Curr. Biol. *23*, 2452–2462. https://doi.org/10.1016/j.cub.2013.09.058.

833 10. Schramm, F.D., Schroeder, K., and Jonas, K. (2020). Protein aggregation in bacteria. FEMS
834 Microbiol. Rev. *44*, 54–72. https://doi.org/10.1093/femsre/fuz026.

835 11. Schäfer, H., Heinz, A., Sudzinová, P., Voß, M., Hantke, I., Krásný, L., and Turgay, K. (2018). Spx,
836 the central regulator of the heat and oxidative stress response in *B. subtilis* , can repress
837 transcription of translation-related genes. Mol. Microbiol., mmi.14171.
838 https://doi.org/10.1111/mmi.14171.

839 12. Nakano, S., Erwin, K.N., Ralle, M., and Zuber, P. (2005). Redox-sensitive transcriptional control
840 by a thiol/disulphide switch in the global regulator, Spx. Mol. Microbiol. *55*, 498–510.
841 https://doi.org/10.1111/j.1365-2958.2004.04395.x.

842 13. Runde, S., Molière, N., Heinz, A., Maisonneuve, E., Janczikowski, A., Elsholz, A.K.W., Gerth, U.,
843 Hecker, M., and Turgay, K. (2014). The role of thiol oxidative stress response in heat-induced
844 protein aggregate formation during thermotolerance in *Bacillus subtilis*. Mol. Microbiol. *91*, 1036–
845 1052. https://doi.org/10.1111/mmi.12521.

846 14. Rochat, T., Nicolas, P., Delumeau, O., Rabatinová, A., Korelusová, J., Leduc, A., Bessières, P.,
847 Dervyn, E., Krásný, L., and Noirot, P. (2012). Genome-wide identification of genes directly
848 regulated by the pleiotropic transcription factor Spx in *Bacillus subtilis*. Nucleic Acids Res. *40*,
849 9571–9583. https://doi.org/10.1093/nar/gks755.

850 15. Diez, S., Ryu, J., Caban, K., Gonzalez, R.L., and Dworkin, J. (2020). The alarmones (p)ppGpp
851 directly regulate translation initiation during entry into quiescence. Proc. Natl. Acad. Sci. *117*,
852 15565–15572. https://doi.org/10.1073/pnas.1920013117.

853 16. Corrigan, R.M., Bellows, L.E., Wood, A., and Gründling, A. (2016). ppGpp negatively impacts
854 ribosome assembly affecting growth and antimicrobial tolerance in Gram-positive bacteria. Proc.
855 Natl. Acad. Sci. *113*. https://doi.org/10.1073/pnas.1522179113.

856 17. Pausch, P., Steinchen, W., Wieland, M., Klaus, T., Freibert, S.-A., Altegoer, F., Wilson, D.N., and
857 Bange, G. (2018). Structural basis for (p)ppGpp-mediated inhibition of the GTPase RbgA. J. Biol.
858 Chem. *293*, 19699–19709. https://doi.org/10.1074/jbc.RA118.003070.

859 18. Krásný, L., Tišerová, H., Jonák, J., Rejman, D., and Šanderová, H. (2008). The identity of the
860 transcription +1 position is crucial for changes in gene expression in response to amino acid
861 starvation in *Bacillus subtilis*. Mol. Microbiol. *69*, 42–54. https://doi.org/10.1111/j.1365-
862 2958.2008.06256.x.

863 19. Krásný, L., and Gourse, R.L. (2004). An alternative strategy for bacterial ribosome synthesis:
864 *Bacillus subtilis* rRNA transcription regulation. EMBO J. *23*, 4473–4483.
865 https://doi.org/10.1038/sj.emboj.7600423.

866 20. Koo, B.-M., Kritikos, G., Farelli, J.D., Todor, H., Tong, K., Kimsey, H., Wapinski, I., Galardini, M.,
867 Cabal, A., Peters, J.M., et al. (2017). Construction and analysis of two genome-scale deletion
868 libraries for *Bacillus subtilis*. Cell Syst. *4*, 291-305.e7. https://doi.org/10.1016/j.cels.2016.12.013.

869 21. Msadek, T., Dartois, V., Kunst, F., Herbaud, M.-L., Denizot, F., and Rapoport, G. (1998). ClpP of
870 *Bacillus subtilis* is required for competence development, motility, degradative enzyme synthesis,
871 growth at high temperature and sporulation. Mol. Microbiol. *27*, 899–914.
872 https://doi.org/10.1046/j.1365-2958.1998.00735.x.

873 22. Hajdusits, B., Suskiewicz, M.J., Hundt, N., Meinhart, A., Kurzbauer, R., Leodolter, J., Kukura, P.,
874 and Clausen, T. (2021). McsB forms a gated kinase chamber to mark aberrant bacterial proteins
875 for degradation. eLife *10*, e63505. https://doi.org/10.7554/eLife.63505.

876 23. Matavacas, J., Hallgren, J., and von Wachenfeldt, C. (2023). *Bacillus subtilis* forms twisted cells
877 with cell wall integrity defects upon removal of the molecular chaperones DnaK and trigger factor.
878 Front. Microbiol. *13*. https://doi.org/10.3389/fmicb.2022.988768.

879 24. Schumann, W. (2016). Regulation of bacterial heat shock stimulons. Cell Stress Chaperones *21*,
880 959–968. https://doi.org/10.1007/s12192-016-0727-z.

881 25. DeLoughery, A., Dengler, V., Chai, Y., and Losick, R. (2016). Biofilm formation by *Bacillus subtilis*
882 requires an endoribonuclease-containing multisubunit complex that controls mRNA levels for the
883 matrix gene repressor SinR. Mol. Microbiol. *99*, 425–437. https://doi.org/10.1111/mmi.13240.

884 26. DeLoughery, A., Lalanne, J.-B., Losick, R., and Li, G.-W. (2018). Maturation of polycistronic
885 mRNAs by the endoribonuclease RNase Y and its associated Y-complex in *Bacillus subtilis*. Proc.
886 Natl. Acad. Sci. *115*, E5585–E5594. https://doi.org/10.1073/pnas.1803283115.

887 27. Broglia, L., Lécrivain, A.-L., Renault, T.T., Hahnke, K., Ahmed-Begrich, R., Le Rhun, A., and
888 Charpentier, E. (2020). An RNA-seq based comparative approach reveals the transcriptome-wide
889 interplay between 3′-to-5′ exoRNases and RNase Y. Nat. Commun. *11*, 1587.
890 https://doi.org/10.1038/s41467-020-15387-6.

891 28. Taggart, J.C., Dierksheide, K.J., LeBlanc, H.J., Lalanne, J.-B., Durand, S., Braun, F., Condon, C.,
892 and Li, G.-W. (2025). A high-resolution view of RNA endonuclease cleavage in *Bacillus subtilis*.
893 Nucleic Acids Res. *53*, gkaf030. https://doi.org/10.1093/nar/gkaf030.

894 29. Khemici, V., Prados, J., Linder, P., and Redder, P. (2015). Decay-initiating endoribonucleolytic
895 cleavage by RNase Y is kept under tight control via sequence preference and sub-cellular
896 localisation. PLOS Genet. *11*, e1005577. https://doi.org/10.1371/journal.pgen.1005577.

897 30. Le Scornet, A., Jousselin, A., Baumas, K., Kostova, G., Durand, S., Poljak, L., Barriot, R.,
898 Coutant, E., Pigearias, R., Tejero, G., et al. (2024). Critical factors for precise and efficient RNA
899 cleavage by RNase Y in *Staphylococcus aureus*. PLOS Genet. *20*, e1011349.
900 https://doi.org/10.1371/journal.pgen.1011349.

901 31. Shahbabian, K., Jamalli, A., Zig, L., and Putzer, H. (2009). RNase Y, a novel endoribonuclease,
902 initiates riboswitch turnover in *Bacillus subtilis*. EMBO J. *28*, 3523–3533.
903 https://doi.org/10.1038/emboj.2009.283.

904 32. Chao, Y., Li, L., Girodat, D., Förstner, K.U., Said, N., Corcoran, C., Śmiga, M., Papenfort, K.,
905 Reinhardt, R., Wieden, H.-J., et al. (2017). In vivo cleavage map illuminates the central role of
906 RNase E in coding and non-coding RNA pathways. Mol. Cell *65*, 39–51.
907 https://doi.org/10.1016/j.molcel.2016.11.002.

908 33. Kime, L., Jourdan, S.S., Stead, J.A., Hidalgo-Sastre, A., and McDowall, K.J. (2010). Rapid
909 cleavage of RNA by RNase E in the absence of 5′ monophosphate stimulation. Mol. Microbiol. *76*,
910 590–604. https://doi.org/10.1111/j.1365-2958.2009.06935.x.

911 34. Davis, J.H., and Williamson, J.R. (2017). Structure and dynamics of bacterial ribosome
912 biogenesis. Philos. Trans. R. Soc. B Biol. Sci. *372*, 20160181.
913 https://doi.org/10.1098/rstb.2016.0181.

914 35. Eymann, C., Homuth, G., Scharf, C., and Hecker, M. (2002). *Bacillus subtilis* functional genomics:
915 global characterization of the stringent response by proteome and transcriptome analysis. J.
916 Bacteriol. *184*, 2500–2520. https://doi.org/10.1128/JB.184.9.2500-2520.2002.

917 36. Tagami, K., Nanamiya, H., Kazo, Y., Maehashi, M., Suzuki, S., Namba, E., Hoshiya, M., Hanai,
918 R., Tozawa, Y., Morimoto, T., et al. (2012). Expression of a small (p)ppGpp synthetase, YwaC, in
919 the (p)ppGpp^0 mutant of *Bacillus subtilis* triggers YvyD-dependent dimerization of ribosome.
920 MicrobiologyOpen *1*, 115–134. https://doi.org/10.1002/mbo3.16.

921 37. Beckert, B., Abdelshahid, M., Schäfer, H., Steinchen, W., Arenz, S., Berninghausen, O.,
922 Beckmann, R., Bange, G., Turgay, K., and Wilson, D.N. (2017). Structure of the *Bacillus subtilis*
923 hibernating 100S ribosome reveals the basis for 70S dimerization. EMBO J. *36*, 2061–2072.
924 https://doi.org/10.15252/embj.201696189.

925 38. Carabetta, V.J., Tanner, A.W., Greco, T.M., Defrancesco, M., Cristea, I.M., and Dubnau, D.
926 (2013). A complex of YlbF, YmcA and YaaT regulates sporulation, competence and biofilm
927 formation by accelerating the phosphorylation of Spo0A. Mol. Microbiol. *88*, 283–300.
928 https://doi.org/10.1111/mmi.12186.

929 39. Tortosa, P., Albano, M., and Dubnau, D. (2000). Characterization of *ylbF*, a new gene involved in
930 competence development and sporulation in *Bacillus subtilis*. Mol. Microbiol. *35*, 1110–1119.
931 https://doi.org/10.1046/j.1365-2958.2000.01779.x.

932 40. Branda, S.S., González-Pastor, J.E., Dervyn, E., Ehrlich, S.D., Losick, R., and Kolter, R. (2004).
933 Genes involved in formation of structured multicellular communities by *Bacillus subtilis*. J.
934 Bacteriol. *186*, 3970–3979. https://doi.org/10.1128/jb.186.12.3970-3979.2004.

935 41. Segev, E., Smith, Y., and Ben-Yehuda, S. (2012). RNA dynamics in aging bacterial spores. Cell
936 *148*, 139–149. https://doi.org/10.1016/j.cell.2011.11.059.

937 42. Dubnau, E., DeSantis, M., and Dubnau, D. (2023). Formation of a stable RNase Y-RicT (YaaT)
938 complex requires RicA (YmcA) and RicF (YlbF). mBio, e01269-23.
939 https://doi.org/10.1128/mbio.01269-23.

940 43. Hinrichs, R., Pozhydaieva, N., Höfer, K., and Graumann, P.L. (2022). Y-complex proteins show
941 RNA-dependent binding events at the cell membrane and distinct single-molecule dynamics. Cells
942 *11*, 933. https://doi.org/10.3390/cells11060933.

943 44. Adusei-Danso, F., Khaja, F.T., DeSantis, M., Jeffrey, P.D., Dubnau, E., Demeler, B., Neiditch,
944 M.B., and Dubnau, D. (2019). Structure-function studies of the *Bacillus subtilis* Ric proteins
945 identify the Fe-S cluster-ligating residues and their roles in development and RNA processing.
946 mBio *10*, e01841-19, /mbio/10/5/mBio.01841-19.atom. https://doi.org/10.1128/mBio.01841-19.

947 45. Lehnik-Habrink, M., Pförtner, H., Rempeters, L., Pietack, N., Herzberg, C., and Stülke, J. (2010).
948 The RNA degradosome in *Bacillus subtilis*: identification of CshA as the major RNA helicase in the
949 multiprotein complex. Mol. Microbiol. *77*, 958–971. https://doi.org/10.1111/j.1365-
950 2958.2010.07264.x.

951 46. Commichau, F.M., Rothe, F.M., Herzberg, C., Wagner, E., Hellwig, D., Lehnik-Habrink, M.,
952 Hammer, E., Völker, U., and Stülke, J. (2009). Novel activities of glycolytic enzymes in *Bacillus*
953 *subtilis*. Mol. Cell. Proteomics *8*, 1350–1360. https://doi.org/10.1074/mcp.M800546-MCP200.

954 47. Durand, S., and Condon, C. RNases and helicases in Gram-positive bacteria. Microbiol. Spectr. *6*,
955 10.1128/microbiolspec.rwr-0003–2017. https://doi.org/10.1128/microbiolspec.rwr-0003-2017.

956 48. Dimitrova-Paternoga, L., Kasvandik, S., Beckert, B., Granneman, S., Tenson, T., Wilson, D.N.,
957 and Paternoga, H. (2024). Structural basis of ribosomal 30S subunit degradation by RNase R.
958 Nature *626*, 1133–1140. https://doi.org/10.1038/s41586-024-07027-6.

959 49. Boylan, S.A., Redfield, A.R., Brody, M.S., and Price, C.W. (1993). Stress-induced activation of the
960 Sigma B transcription factor of *Bacillus subtilis*. J. Bacteriol. *175*, 7931–7937.
961 https://doi.org/10.1128/jb.175.24.7931-7937.1993.

962 50. Trentini, D.B., Suskiewicz, M.J., Heuck, A., Kurzbauer, R., Deszcz, L., Mechtler, K., and Clausen,
963 T. (2016). Arginine phosphorylation marks proteins for degradation by a Clp protease. Nature *539*,
964 48–53. https://doi.org/10.1038/nature20122.

965 51. Schmidt, A., Trentini, D.B., Spiess, S., Fuhrmann, J., Ammerer, G., Mechtler, K., and Clausen, T.
966 (2014). Quantitative phosphoproteomics reveals the role of protein arginine phosphorylation in the
967 bacterial stress response. Mol. Cell. Proteomics *13*, 537–550.
968 https://doi.org/10.1074/mcp.M113.032292.

969 52. Elsholz, A.K.W., Turgay, K., Michalik, S., Hessling, B., Gronau, K., Oertel, D., Mäder, U.,
970 Bernhardt, J., Becher, D., Hecker, M., et al. (2012). Global impact of protein arginine
971 phosphorylation on the physiology of *Bacillus subtilis*. Proc. Natl. Acad. Sci. *109*, 7451–7456.
972 https://doi.org/10.1073/pnas.1117483109.

973 53. Lytvynenko, I., Paternoga, H., Thrun, A., Balke, A., Müller, T.A., Chiang, C.H., Nagler, K.,
974 Tsaprailis, G., Anders, S., Bischofs, I., et al. (2019). Alanine tails signal proteolysis in bacterial
975 ribosome-associated quality control. Cell *178*, 76-90.e22.
976 https://doi.org/10.1016/j.cell.2019.05.002.

977 54. Wiegert, T., and Schumann, W. (2001). SsrA-mediated tagging in *Bacillus subtilis*. J. Bacteriol.
978 *183*, 3885–3889. https://doi.org/10.1128/JB.183.13.3885-3889.2001.

979 55. Lehnik-Habrink, M., Schaffer, M., Mäder, U., Diethmaier, C., Herzberg, C., and Stülke, J. (2011).
980 RNA processing in *Bacillus subtilis*: identification of targets of the essential RNase Y: Targets of
981 the essential RNase Y in *Bacillus subtilis*. Mol. Microbiol. *81*, 1459–1473.
982 https://doi.org/10.1111/j.1365-2958.2011.07777.x.

983 56. Anderson, B.W., Fung, D.K., and Wang, J.D. (2021). Regulatory themes and variations by the
984 stress-signaling nucleotide alarmones (p)ppGpp in bacteria. Annu. Rev. Genet. *55*, 115–133.
985 https://doi.org/10.1146/annurev-genet-021821-025827.

986 57. Driller, K., Cornejo, F.A., and Turgay, K. (2023). (p)ppGpp – an important player during heat
987 shock response. microLife *4*, uqad017. https://doi.org/10.1093/femsml/uqad017.

988 58. Zundel, M.A., Basturea, G.N., and Deutscher, M.P. (2009). Initiation of ribosome degradation
989 during starvation in *Escherichia coli*. RNA *15*, 977–983. https://doi.org/10.1261/rna.1381309.

990 59. Sulthana, S., Basturea, G.N., and Deutscher, M.P. (2016). Elucidation of pathways of ribosomal
991 RNA degradation: an essential role for RNase E. RNA *22*, 1163–1171.
992 https://doi.org/10.1261/rna.056275.116.

993 60. Lehnik-Habrink, M., Newman, J., Rothe, F.M., Solovyova, A.S., Rodrigues, C., Herzberg, C.,
994 Commichau, F.M., Lewis, R.J., and Stulke, J. (2011). RNase Y in *Bacillus subtilis*: a natively
995 disordered protein that is the functional equivalent of RNase E from *Escherichia coli*. J. Bacteriol.
996 *193*, 5431–5441. https://doi.org/10.1128/JB.05500-11.

997 61. Marcaida, M.J., DePristo, M.A., Chandran, V., Carpousis, A.J., and Luisi, B.F. (2006). The RNA
998 degradosome: life in the fast lane of adaptive molecular evolution. Trends Biochem. Sci. *31*, 359–
999 365. https://doi.org/10.1016/j.tibs.2006.05.005.

1000 62. Piir, K., Paier, A., Liiv, A., Tenson, T., and Maiväli, Ü. (2011). Ribosome degradation in growing
1001 bacteria. EMBO Rep. *12*, 458–462. https://doi.org/10.1038/embor.2011.47.

1002 63. Kuroda, A., Nomura, K., Ohtomo, R., Kato, J., Ikeda, T., Takiguchi, N., Ohtake, H., and Kornberg,
1003 A. (2001). Role of inorganic polyphosphate in promoting ribosomal protein degradation by the Lon
1004 protease in *E. coli*. Science *293*, 705–708. https://doi.org/10.1126/science.1061315.

1005 64. An, H., and Harper, J.W. (2020). Ribosome abundance control via the ubiquitin–proteasome
1006 system and autophagy. J. Mol. Biol. *432*, 170–184. https://doi.org/10.1016/j.jmb.2019.06.001.

1007 65. Huang, Z., Diehl, F.F., Wang, M., Li, Y., Song, A., Chen, F.X., Rosa-Mercado, N.A., Beckmann,
1008 R., Green, R., and Cheng, J. (2025). RIOK3 mediates the degradation of 40S ribosomes. Mol.
1009 Cell *85*, 802-814.e12. https://doi.org/10.1016/j.molcel.2025.01.013.

1010 66. Ford, P.W., Garshott, D.M., Narasimhan, M., Ge, X., Jordahl, E.M., Subramanya, S., and Bennett,
1011 E.J. (2025). RNF10 and RIOK3 facilitate 40S ribosomal subunit degradation upon 60S biogenesis
1012 disruption or amino acid starvation. Cell Rep. *44*, 115371.
1013 https://doi.org/10.1016/j.celrep.2025.115371.

1014 67. Coria, A.R., Shah, A., Shafieinouri, M., Taylor, S.J., Orgebin, E., Guiblet, W., Miller, J.T., Sharma,
1015 I.M., and Wu, C.C.-C. (2025). The integrated stress response regulates 18S nonfunctional rRNA
1016 decay in mammals. Mol. Cell *85*, 787-801.e8. https://doi.org/10.1016/j.molcel.2025.01.017.

1017 68. Simpkins, S.W., Deshpande, R., Nelson, J., Li, S.C., Piotrowski, J.S., Ward, H.N., Yashiroda, Y.,
1018 Osada, H., Yoshida, M., Boone, C., et al. (2019). Using BEAN-counter to quantify genetic
1019 interactions from multiplexed barcode sequencing experiments. Nat. Protoc. *14*, 415–440.
1020 https://doi.org/10.1038/s41596-018-0099-1.

1021 69. Benjamini, Y., and Hochberg, Y. (1995). Controlling the false discovery rate: a practical and
1022 powerful approach to multiple testing. J. R. Stat. Soc. Ser. B Methodol. *57*, 289–300.
1023 https://doi.org/10.1111/j.2517-6161.1995.tb02031.x.

1024 70. Lécrivain, A.-L., Le Rhun, A., Renault, T.T., Ahmed-Begrich, R., Hahnke, K., and Charpentier, E.
1025 (2018). In vivo 3′-to-5′ exoribonuclease targetomes of *Streptococcus pyogenes*. Proc. Natl. Acad.
1026 Sci. *115*, 11814–11819. https://doi.org/10.1073/pnas.1809663115.

1027 71. Martin, M. (2011). Cutadapt removes adapter sequences from high-throughput sequencing reads.
1028 EMBnet.journal *17*, 10. https://doi.org/10.14806/ej.17.1.200.

1029 72. Dobin, A., Davis, C.A., Schlesinger, F., Drenkow, J., Zaleski, C., Jha, S., Batut, P., Chaisson, M.,
1030 and Gingeras, T.R. (2013). STAR: ultrafast universal RNA-seq aligner. Bioinformatics *29*, 15–21.
1031 https://doi.org/10.1093/bioinformatics/bts635.

1032 73. Li, H., Handsaker, B., Wysoker, A., Fennell, T., Ruan, J., Homer, N., Marth, G., Abecasis, G.,
1033 Durbin, R., and 1000 Genome Project Data Processing Subgroup (2009). The Sequence
1034 Alignment/Map format and SAMtools. Bioinformatics *25*, 2078–2079.
1035 https://doi.org/10.1093/bioinformatics/btp352.

1036 74. Smith, T., Heger, A., and Sudbery, I. (2017). UMI-tools: modeling sequencing errors in Unique
1037 Molecular Identifiers to improve quantification accuracy. Genome Res. *27*, 491–499.
1038 https://doi.org/10.1101/gr.209601.116.

1039 75. Liao, Y., Smyth, G.K., and Shi, W. (2014). featureCounts: an efficient general purpose program for
1040 assigning sequence reads to genomic features. Bioinformatics *30*, 923–930.
1041 https://doi.org/10.1093/bioinformatics/btt656.

1042 76. Love, M.I., Huber, W., and Anders, S. (2014). Moderated estimation of fold change and dispersion
1043 for RNA-seq data with DESeq2. Genome Biol. *15*, 550. https://doi.org/10.1186/s13059-014-0550-
1044 8.

1045 77. Putri, G.H., Anders, S., Pyl, P.T., Pimanda, J.E., and Zanini, F. (2022). Analysing high-throughput
1046 sequencing data in Python with HTSeq 2.0. Bioinformatics *38*, 2943–2945.
1047 https://doi.org/10.1093/bioinformatics/btac166.

1048 78. Mölder, F., Jablonski, K.P., Letcher, B., Hall, M.B., Tomkins-Tinch, C.H., Sochat, V., Forster, J.,
1049 Lee, S., Twardziok, S.O., Kanitz, A., et al. (2021). Sustainable data analysis with Snakemake.
1050 Preprint at F1000Research, https://doi.org/10.12688/f1000research.29032.2
1051 https://doi.org/10.12688/f1000research.29032.2.

1052 79. McCarthy, D.J., Chen, Y., and Smyth, G.K. (2012). Differential expression analysis of multifactor
1053 RNA-Seq experiments with respect to biological variation. Nucleic Acids Res. *40*, 4288–4297.
1054 https://doi.org/10.1093/nar/gks042.

1055 80. Geissler, A.S., Anthon, C., Alkan, F., González-Tortuero, E., Poulsen, L.D., Kallehauge, T.B.,
1056 Breüner, A., Seemann, S.E., Vinther, J., and Gorodkin, J. (2021). BSGatlas: a unified *Bacillus*
1057 *subtilis* genome and transcriptome annotation atlas with enhanced information access. Microb.
1058 Genomics *7*, 000524. https://doi.org/10.1099/mgen.0.000524.

1059 81. Tareen, A., and Kinney, J.B. (2020). Logomaker: beautiful sequence logos in Python.
1060 Bioinformatics *36*, 2272–2274. https://doi.org/10.1093/bioinformatics/btz921.

1061 82. Lorenz, R., Bernhart, S.H., Höner zu Siederdissen, C., Tafer, H., Flamm, C., Stadler, P.F., and
1062 Hofacker, I.L. (2011). ViennaRNA Package 2.0. Algorithms Mol. Biol. *6*, 26.
1063 https://doi.org/10.1186/1748-7188-6-26.

1064 83. Elfmann, C., Dumann, V., van den Berg, T., and Stülke, J. (2025). A new framework for SubtiWiki,
1065 the database for the model organism *Bacillus subtilis*. Nucleic Acids Res. *53*, D864–D870.
1066 https://doi.org/10.1093/nar/gkae957.

1067 84. Pfaffl, M.W. (2001). A new mathematical model for relative quantification in real-time RT-PCR.
1068 Nucleic Acids Res. *29*, 45e–445. https://doi.org/10.1093/nar/29.9.e45.

1069 85. Hughes, C.S., Moggridge, S., Müller, T., Sorensen, P.H., Morin, G.B., and Krijgsveld, J. (2019).
1070 Single-pot, solid-phase-enhanced sample preparation for proteomics experiments. Nat. Protoc.
1071 *14*, 68–85. https://doi.org/10.1038/s41596-018-0082-x.

1072 86. Kohler, D., Staniak, M., Tsai, T.-H., Huang, T., Shulman, N., Bernhardt, O.M., MacLean, B.X.,
1073 Nesvizhskii, A.I., Reiter, L., Sabido, E., et al. (2023). MSstats version 4.0: statistical analyses of
1074 quantitative mass spectrometry-based proteomic experiments with chromatography-based
1075 quantification at scale. J. Proteome Res. *22*, 1466–1482.
1076 https://doi.org/10.1021/acs.jproteome.2c00834.

1077 87. Jahn, M., Vialas, V., Karlsen, J., Maddalo, G., Edfors, F., Forsström, B., Uhlén, M., Käll, L., and
1078 Hudson, E.P. (2018). Growth of cyanobacteria is constrained by the abundance of light and
1079 carbon assimilation proteins. Cell Rep. *25*, 478-486.e8.
1080 https://doi.org/10.1016/j.celrep.2018.09.040.

1081 88. Jahn, M., Crang, N., Janasch, M., Hober, A., Forsström, B., Kimler, K., Mattausch, A., Chen, Q.,
1082 Asplund-Samuelsson, J., and Hudson, E.P. (2021). Protein allocation and utilization in the

1083 versatile chemolithoautotroph *Cupriavidus necator*. eLife *10*, e69019.
1084 https://doi.org/10.7554/eLife.69019.

1085 89. Sohmen, D., Chiba, S., Shimokawa-Chiba, N., Innis, C.A., Berninghausen, O., Beckmann, R., Ito,
1086 K., and Wilson, D.N. (2015). Structure of the *Bacillus subtilis* 70S ribosome reveals the basis for
1087 species-specific stalling. Nat. Commun. *6*, 6941. https://doi.org/10.1038/ncomms7941.

1088

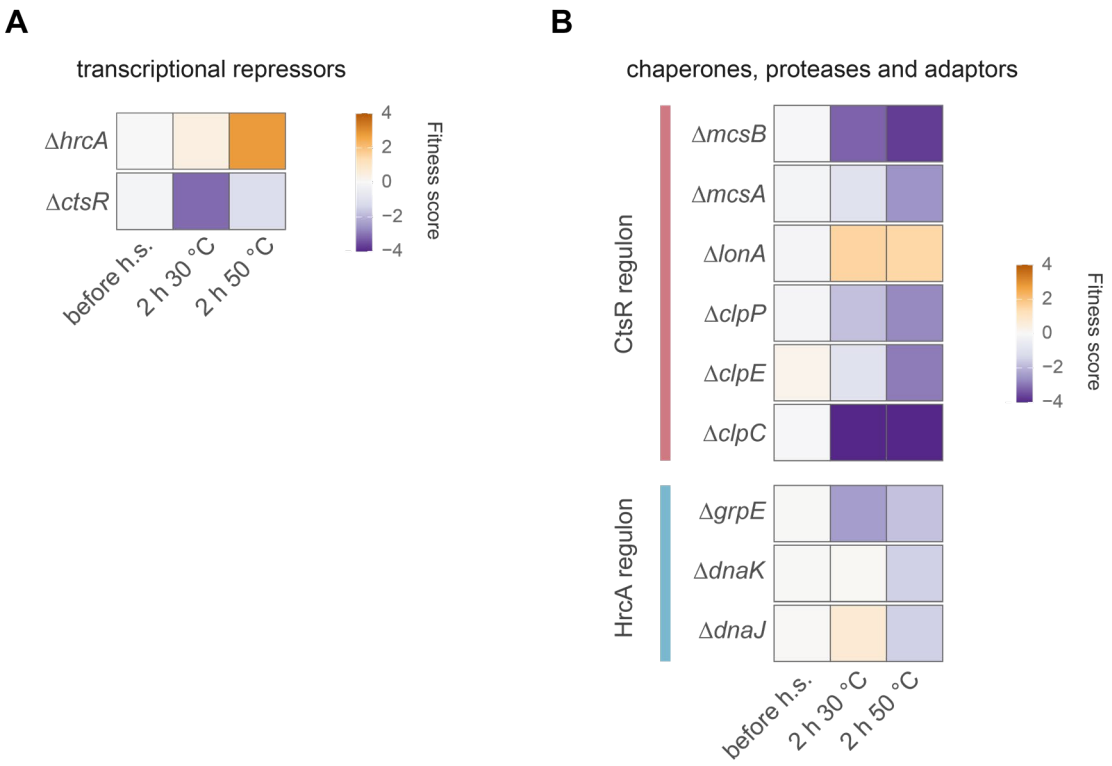

1089

1090 **Figure S1. Fitness of selected deletion mutants during heat shock in the genetic screening.**
1091 Heatmap of the relative fitness of **A)** heat shock transcriptional repressors, and **B)** chaperones,
1092 proteases and adaptors. The color represents the average relative fitness of three biological replicates.
1093 A negative relative fitness value means that the abundance of the deletion mutant, compared to the rest
1094 of the population, was negatively affected by the treatment, while a positive value means an increased
1095 abundance on those conditions. h.s. = heat shock.

1096

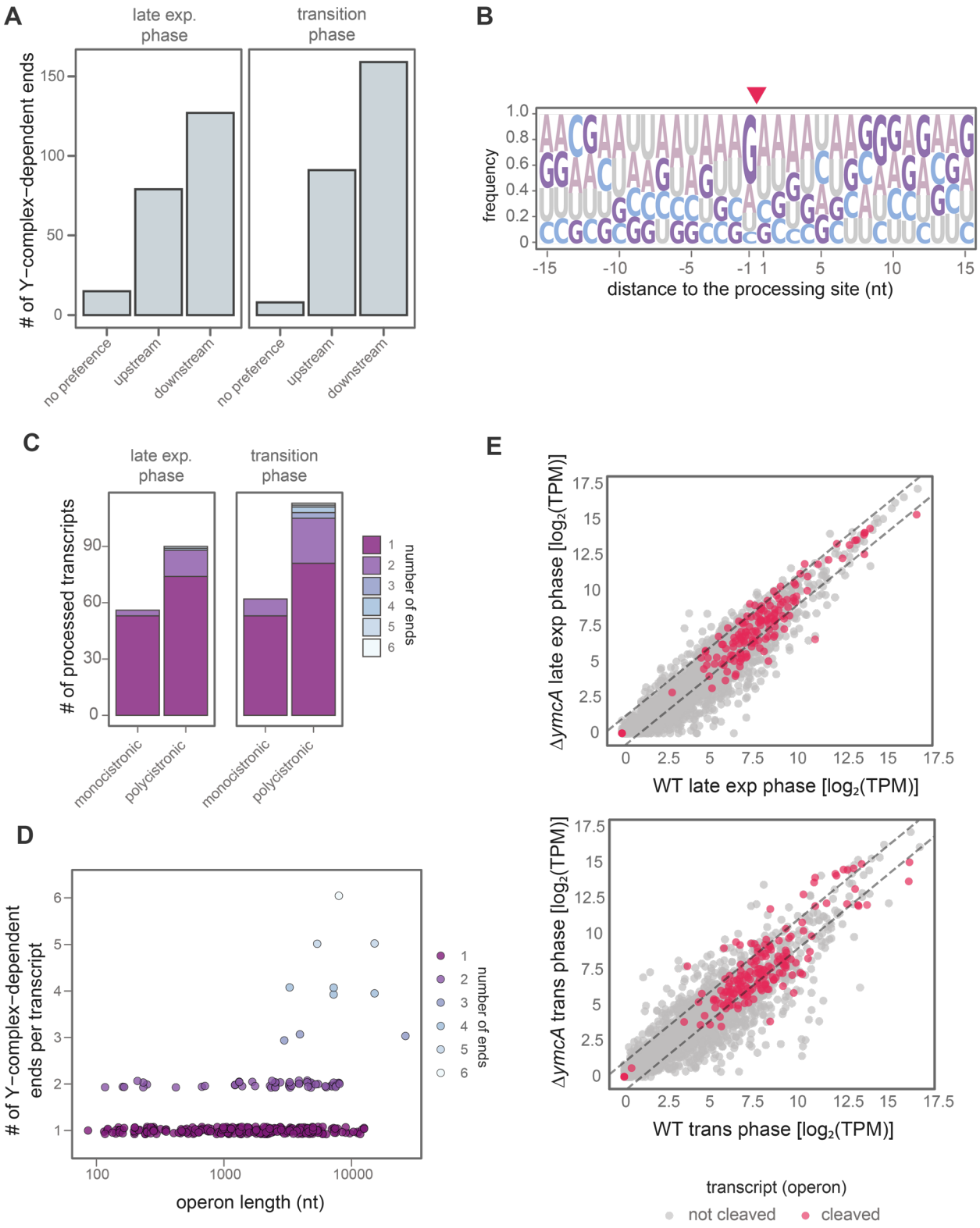

Figure S2. Recognition motif, length, or expression levels do not determine the Y-complex substrates. A) Stabilization of the resulting fragments after Y-complex processing, the coverage ratio in a window of 5 nt before and after the processing site was calculated and used as a proxy of the stabilization of the resulting fragments. The predicted stability correlates with the end detected in the ISCP method. **B)** Motif search using 5' and U-type ends. The arrow indicates the cleavage site. **C)** Number of Y-complex-dependent cleavages detected per monocistronic or polycistronic transcripts in the late exponential or transition phase. **D)** Number of cleavages detected by operon length of the

1105 transcript. The color indicates the numbers of Y-complex-dependent ends detected per transcript **E)**
1106 RNA levels of WT and Δ*ymcA* mutant transcripts at late exponential and transition phases. Transcripts
1107 processed by the Y-complex are highlighted in magenta. Transcript annotations were obtained from
1108 BSGatlas.

1109

1110

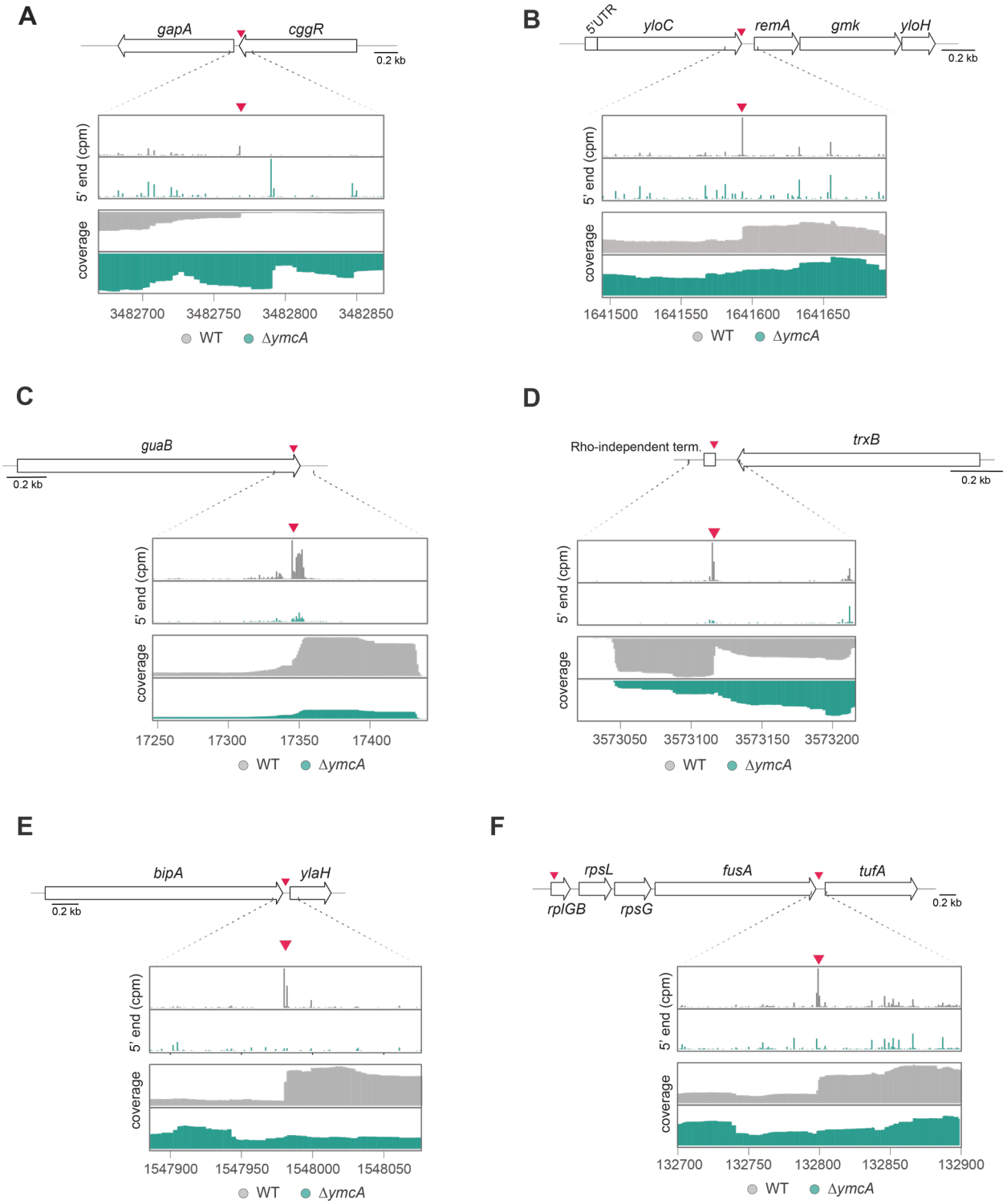

1111

1112 **Figure S3. The Y-complex processes mRNA in UTRs and coding regions.** RNA end counts per
1113 million (cpm), and RNA-seq coverage of selected transcripts in WT and Δ*ymcA*. The arrow indicates the
1114 Y-complex-dependent processing site. **A)** The *gapA-cggR* transcript was used as a positive control. **B)**
1115 Processing in the coding region of *yloC* in the polycistronic mRNA *yloC-remA-gmk-yloH*. **C)** Processing
1116 in the coding region of the monocistronic transcript of *guaB*. **D)** Processing at the 3' UTR of *trxB,* near
1117 the Rho-independent terminator. Processing in the internal UTR of translation-associated transcripts
1118 like **E)** the *bipA-ylaH* transcript, and **F)** between *fusA-tufA*.

1119

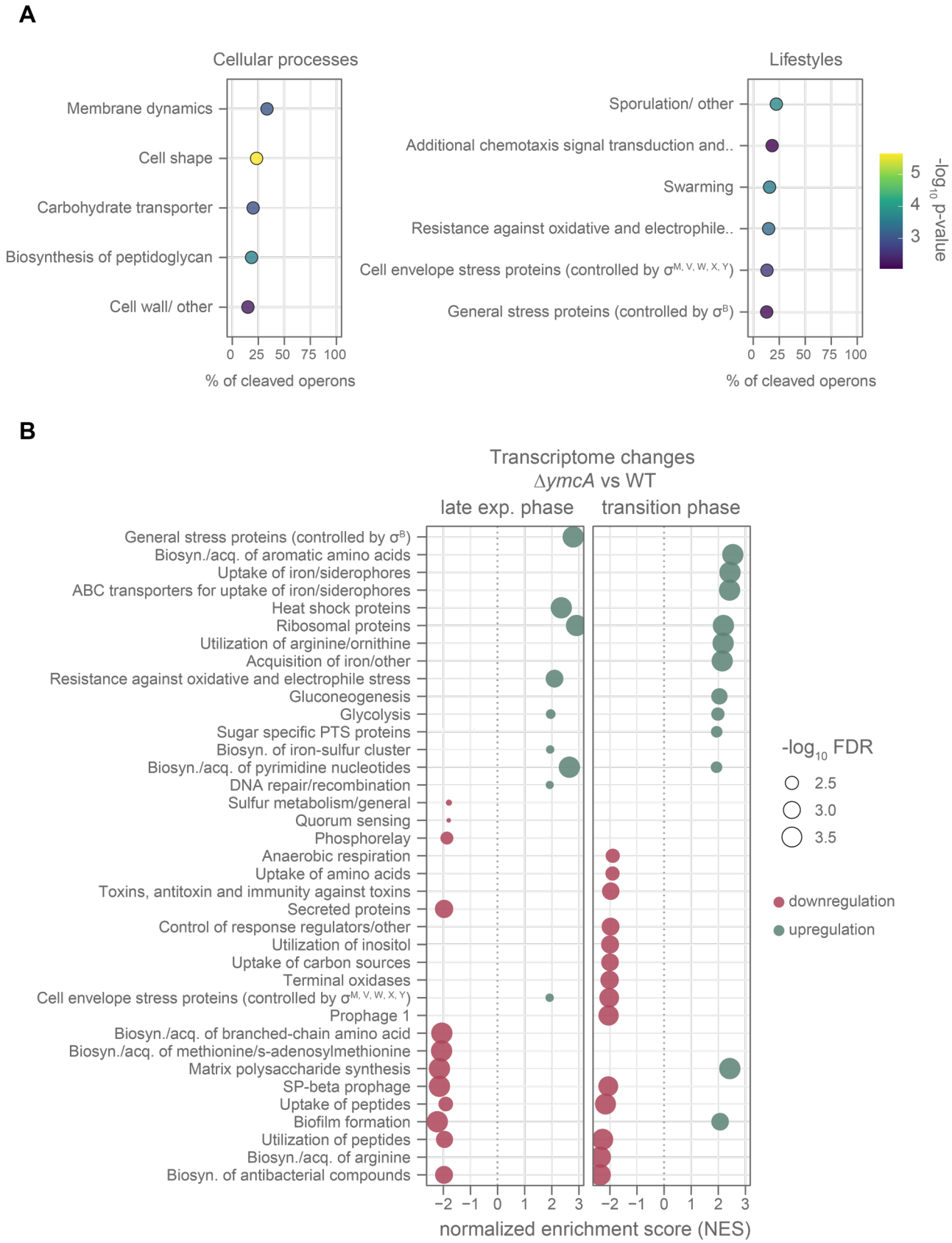

1120

1121 **Figure S4. mRNA processing by the Y-complex and effect on the transcriptome. A)**
1122 Overrepresentation analysis of pathways whose transcripts are cleaved by the Y-complex during the

1123 late exponential phase. Operons were assigned to be involved in a pathway if they code for one gene
1124 participating in such a pathway. Pathway annotations were retrieved from SubtiWiki[83]. The color
1125 indicates the statistical significance of the enrichment. **B)** Gene set enrichment analysis (GSEA) of
1126 differentially expressed genes at the late exponential and transition phase when comparing Δ*ymcA* to
1127 WT. The size of the dot represents the statistical significance. The normalized enrichment score is
1128 displayed on the *x*-axis; positive values mean upregulation; meanwhile negative values mean
1129 downregulation. GSEA results were prefiltered for pathways showing and enrichment with an FDR ≤
1130 0.01. Biosyn. = Biosynthesis, acq. = Acquisition.

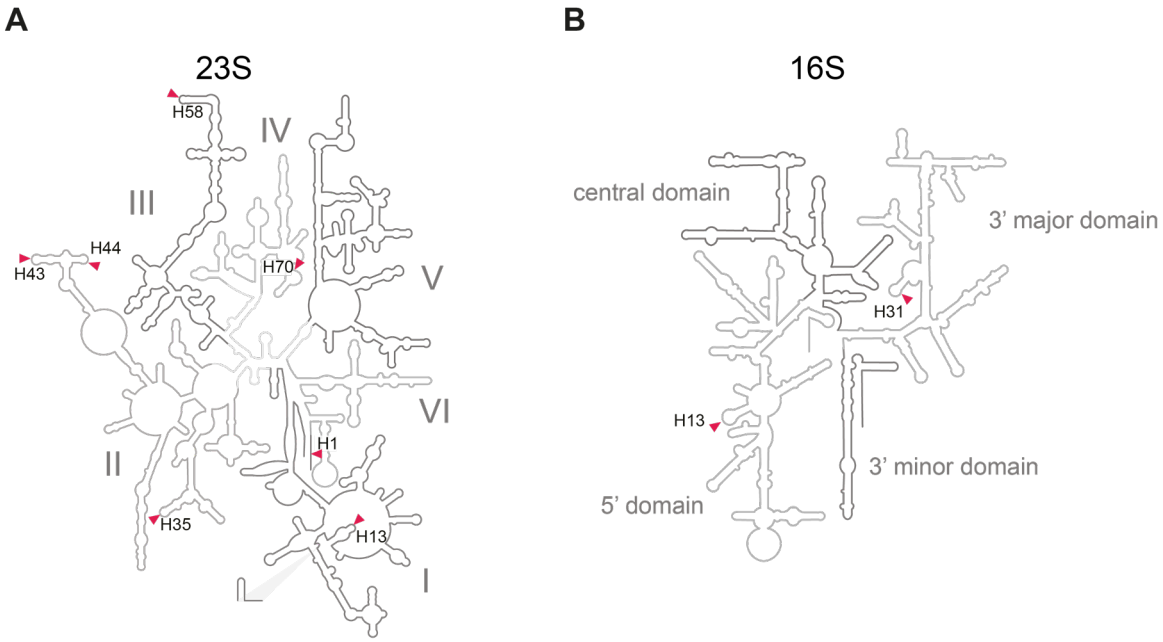

1131

1132 **Figure S5. Mapping of Y-complex-dependent processing in the secondary structure of rRNA at**
1133 **the late exponential phase.** Cleavages are marked with an arrow and the helix number for **A)** 23S and
1134 **B)** 16S rRNA.

1135

Figure S6. Mapping of Y-complex dependent processing in the ribosome 3D structure. The RNA end detected by the ISCP method is highlighted in magenta. The ribosome structure was retrieved from PDB (ID: 3J9W)[89]. The A site is shown as a green ellipse.

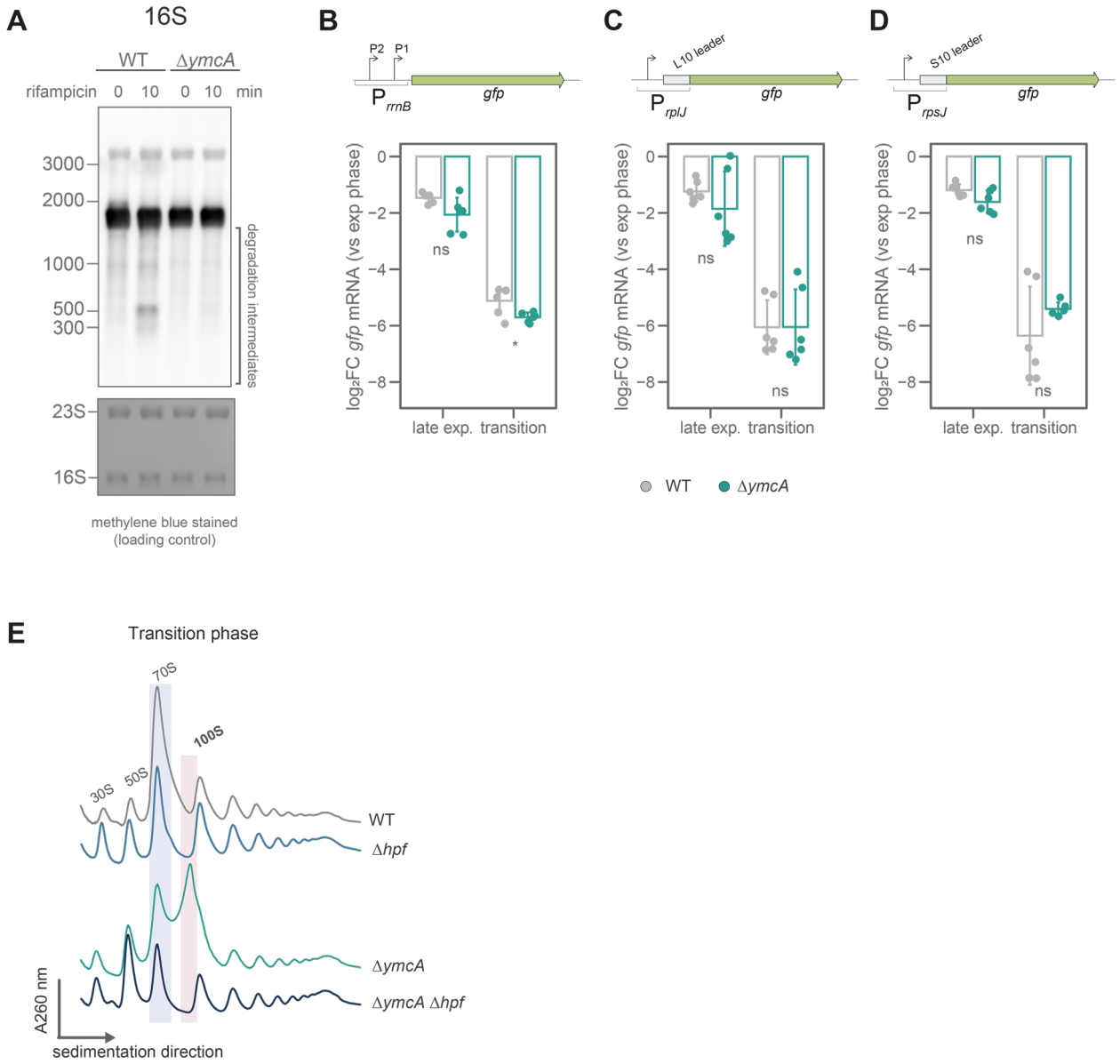

Figure S7. Y-complex-dependent initiates degradation of rRNA but does not affect transcriptional control of stringent response. A) Northern blot against 16S of WT and Δ*ymcA* cells at the late exponential phase, before and after treatment with 100 µg/ml rifampicin to inhibit transcription. The methylene blue-stained membrane is shown as a loading control. This image is representative of three biological replicates. Activity of the promoter controlling **B)** *rrnB* (rRNA) transcription, **C)** *rplJ*, and **D)** *rpsJ* (r-proteins) genes at late exponential and transition phase compared to the exponential phase in WT and Δ*ymcA*. The promoters were cloned controlling *gfp* transcription, which was measured using RT-qPCR. The *pcp* transcript was used as a reference. Individual values and the average ± standard deviation of three biological replicates and two technical replicates are shown. The statistical significance was tested using student's *t*-test. ns: *p*-value > 0.05, *: *p*-value ≤ 0.05. **E)** Ribosome sedimentation profile in 10-50% sucrose gradients of WT, Δ*hpf,* Δ*ymcA,* and Δ*ymcA* Δ*hpf* in the transition phase. The 70S and 100S ribosomes are highlighted with a blue or red box, respectively. The data is representative of three biological replicates.

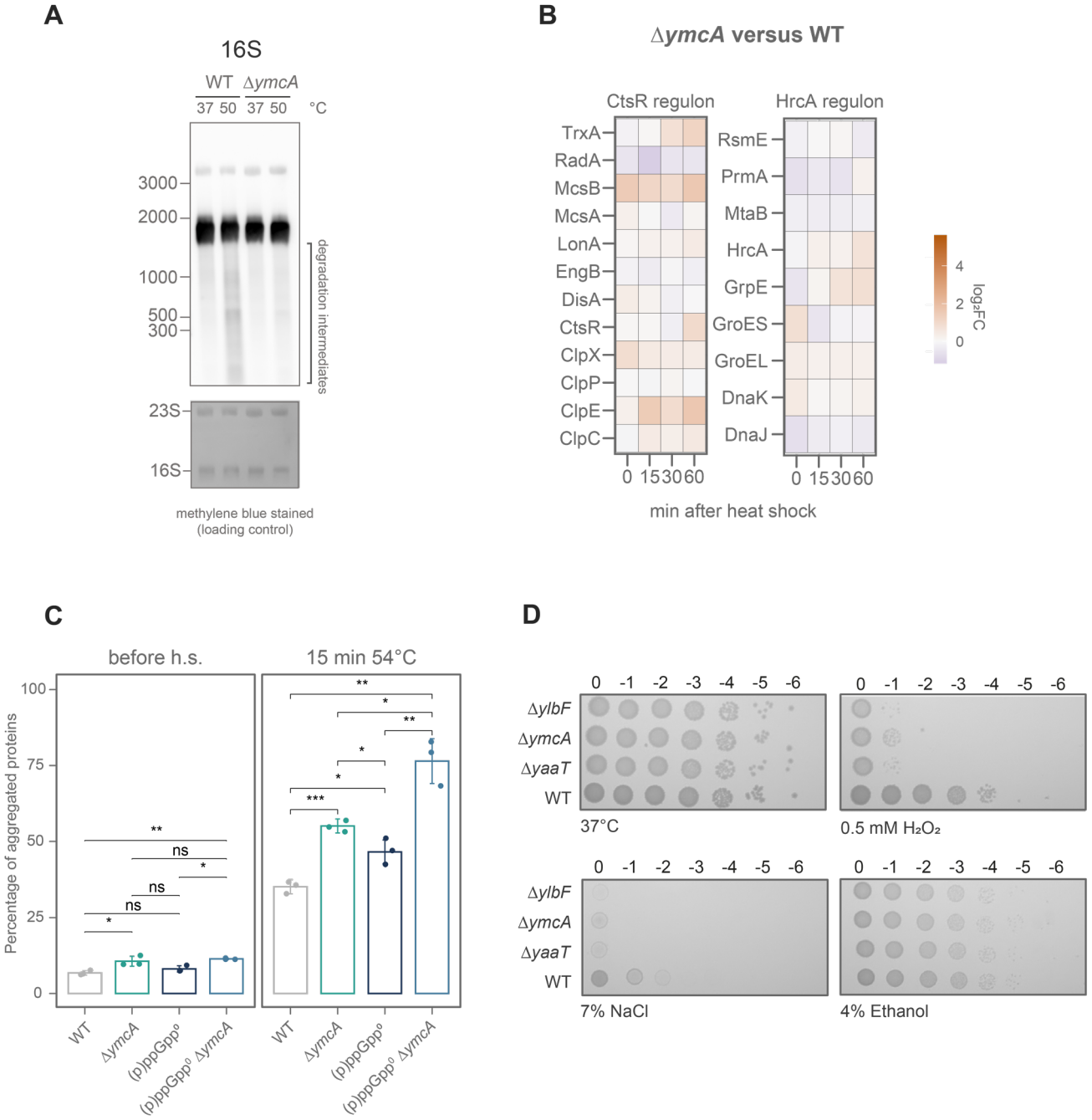

Figure S8. Control of ribosome levels and protein homeostasis in *ymcA* is important for responding against proteotoxic stresses. A) Northern blot against 16S of WT and Δ*ymcA* cells at exponential phase before and after heat shock. The methylene blue-stained membrane is shown as a loading control. This image is representative of three biological replicates. **B)** Induction of CtsR and HrcA regulons after heat shock (50°C) Δ*ymcA* compared to the WT. Proteins were measured by mass spectrometry. The color bar shows the $\log_2$ fold change compared to the WT control. **C)** Percentage of aggregated proteins before and after a 15 min heat shock at 54°C in WT and Δ*ymcA*, (p)ppGpp^0 and (p)ppGpp^0 Δ*ymcA*. Individual values and the average ± standard deviation of three biological replicates are shown. The statistical difference was tested using student's *t*-test. ns: *p*-value > 0.05, *: *p*-value ≤ 0.05, **: *p*-value ≤ 0.01, ***: *p*-value ≤ 0.001. **D)** Spot test of deletion mutants of Y-complex members in the displayed stresses. The picture is representative of three biological replicates.